



# Radial-velocity variation of a tertiary star orbiting a binary black hole in coplanar and noncoplanar triples: short- and long-term anomalous behavior

TOSHINORI HAYASHI <sup>1</sup> AND YASUSHI SUTO <sup>1,2</sup>

<sup>1</sup>*Department of Physics, The University of Tokyo, Tokyo 113-0033, Japan*

<sup>2</sup>*Research Center for the Early Universe, School of Science, The University of Tokyo, Tokyo 113-0033, Japan*

(Received 2020 February 25; Revised 2020 May 5; Accepted 2020 May 26)

Submitted to ApJ

## ABSTRACT

A number of ongoing surveys are likely to discover star-black hole binaries in our Galaxy in the near future. A fraction of them may be triple systems comprising an inner binary, instead of a single black hole, which might be progenitors of binary black holes (BBHs) routinely discovered now from the gravitational wave. We extend our previous proposal to locate inner BBHs from the short-term radial-velocity (RV) variation of a tertiary star in coplanar triples, and we consider noncoplanar triples and their long-term RV variations as well. Specifically, we assume coplanar and noncoplanar triples with an inner BBH of the total mass  $20 M_{\odot}$ , whose outer and inner orbital periods are 80 days and 10 days, respectively. We perform a series of N-body simulations and compare the results with analytic approximate solutions based on quadrupole perturbation theory. For coplanar triples, the pericenter shift of the outer star can be used to detect the hidden inner BBH. For noncoplanar triples, the total RV semi-amplitude of the outer star is modulated periodically on the order of 100km/s due to its precession over roughly the Kozai-Lidov oscillation timescale. Such long-term modulations would be detectable within a decade, independent of the short-term RV variations on the order of 100 m/s at roughly twice the orbital frequency of the inner binary. Thus the RV monitoring of future star-black hole binary candidates offers a promising method for searching for their inner hidden BBHs in optical bands.

*Keywords:* techniques: radial velocities - celestial mechanics - (stars:) binaries (including multiple): close - stars: black holes

## 1. INTRODUCTION

Astronomy is a science triggered and advanced by a series of surprising discoveries. Well-known examples include black holes (BHs) and neutron stars, which had been *predicted* by physics but regarded for a long time as merely theoretical concepts. No law of physics prohibits the presence

of Hot Jupiters and massive binary BHs (BBHs), but they had not been seriously considered to be detectable in reality, nor even to exist at all. Their discoveries (Mayor & Queloz 1995; Abbott et al. 2016), however, have brought revolutions in astronomy.

A recent discovery of a star–BH binary system, LB-1 (Liu et al. 2019), might be the case as well. The mass of the central BH was originally claimed to be  $68_{-13}^{+11}M_{\odot}$ , which is too large according to conventional theories of BH formation (e.g., Leung et al. 2019). An exciting possibility is that LB-1 is indeed a triple system comprising an inner BBH and an outer orbiting star.

Several subsequent studies pointed out that the original claim should be revised; the mass of the inner BH is more likely to be smaller and between  $5M_{\odot}$  and  $20M_{\odot}$  (Abdul-Masih et al. 2020; El-Badry & Quataert 2020), and the presence of a possible inner BBH in LB-1 is severely constrained (Shen et al. 2019).

While we revised this paper according to the referee report, however, Shenar et al. (2020) reported that LB-1 is unlikely to contain a BH, but rather consists of a stripped primary star of  $\sim 1.5 M_{\odot}$  and a fast-rotating B3 Ve star of  $\sim 7 M_{\odot}$  from their latest spectra observed with HERMES and FEROS. Throughout this paper, we still adopt the set of parameters for triples inspired from the parameters originally estimated by Liu et al. (2019), Abdul-Masih et al. (2020), and El-Badry & Quataert (2020). Nevertheless, our results presented below are applicable to the star-BH binaries with similar architecture in general, and provide useful strategies for searching for BBHs.

Since it is quite possible that our Galaxy hosts abundant star-BH binaries, there are many proposals to search for star-BH binaries with *Gaia* (e.g. Brevik et al. 2017; Kawanaka et al. 2016; Mashian & Loeb 2017; Yamaguchi et al. 2018; Shikauchi et al. 2020) and *TESS* (e.g. Masuda & Hotokezaka 2019) among others. A number of such star–BH binaries are likely to be detected in the near future, and a fraction of them may turn out to be a star – BBH triple in reality.

Observationally, more than 70 percent of OBA stars and 50 percent of KGF stars are in binaries or higher multiples (Raghavan et al. 2010; Sana et al. 2012). Rose et al. (2019), for instance, performed secular simulations of triples, assuming many initial distribution models for orbital parameters. They found that the final inner-period distribution after 10 Myr is statistically consistent with the observed distribution of massive binaries in Sana et al. (2012) and Kobulnicky et al. (2014). Thus, it is indeed possible that there are abundant triple systems consisting of a star and an inner compact binary.

Our previous paper (Hayashi et al. 2020, hereafter Paper I), showed that the short-term radial velocity (RV) variations provide a useful probe of a hidden inner BBH in a coplanar triple system. The present paper extends the work, and considers the noncoplanar and unequal mass cases as well. We perform a series of N-body simulations, and model the resulting RV variations by generalizing analytic formulae based on the quadrupole perturbation theory (Morais & Correia 2008). For coplanar triples, we find that the precession of the argument of pericenter is a useful probe of an inner hidden binary. For noncoplanar triples, the long-term variations of the RV semi-amplitude induced by the nodal precession and the Kozai-Lidov oscillation can be used to search for an inner binary, as can the short-term RV variations.

The rest of the paper is organized as follows. Section 2 presents stability constraints on an inner BBH for a hypothetical star-BBH triple inspired by the set of parameters originally proposed for the LB-1 system (Liu et al. 2019), using the approximate RV formula in coplanar orbits by Morais & Correia (2008).

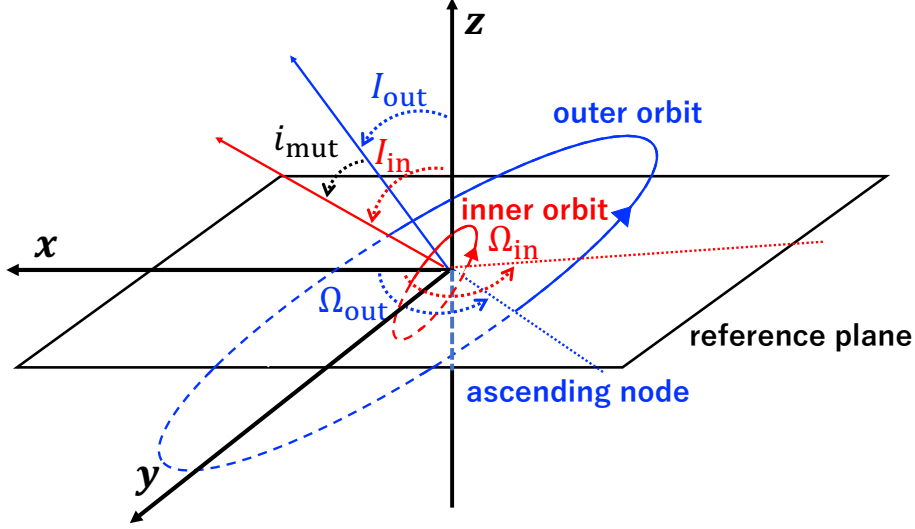


**Figure 1.** Schematic illustration of a triple system that we consider in the present paper. The orbital angles are defined with respect to the reference Cartesian frame whose origin is set to be the barycenter of the inner orbit.

Then we predict the RV variations of the outer star around the inner BBH in section 3. We first consider coplanar orbits, and find that the numerical results are reasonably well reproduced by the analytic approximation for the residual RV velocity component by [Morais & Correia \(2008\)](#) and [Morais & Correia \(2011\)](#) even including the eccentricity effect as long as the quasi-Keplerian motion is extracted properly. Next we examine noncoplanar cases from numerical simulations. Due to the precession of the inner and outer orbits in noncoplanar systems, the amplitude of the stellar RV changes significantly over roughly the Kozai-Lidov timescale. In section 4, we discuss possible effects of the general relativistic correction on the orbital evolution, and also possible formation channels of star-BBH triples. Section 5 is devoted to the conclusions of this paper. Appendix A discusses the long-term behavior of noncoplanar star-BBH triples on the basis of the secular perturbation theory.

## 2. CONSTRAINTS ON A POSSIBLE INNER BINARY IN THE HYPOTHETICAL TRIPLE INSPIRED BY THE PREVIOUS ESTIMATE FOR THE LB-1 SYSTEM

Figure 1 shows a schematic configuration of a triple system consisting of an inner BBH and an outer orbiting star. In what follows, we use the subscript  $j$  ( $=$  in and out) to distinguish between those variables of the inner and outer orbits, respectively. With respect to the reference coordinate system, the inner and outer orbits are specified by the instantaneous longitudes of the ascending nodes  $\Omega_j$ , semi-major axes  $a_j$ , eccentricities  $e_j$ , arguments of pericenter  $\omega_j$ , orbital inclinations  $I_j$ , and their mutual inclination  $i_{\text{mut}}$ . Note that our reference plane in Figure 1 is arbitrary while it is often chosen as the invariant plane of the triple system.

In the case of a coplanar and near-circular hierarchical triple system, [Morais & Correia \(2008\)](#) found that the RV of an outer star ( $m_*$ ) orbiting an inner binary ( $m_1$  and  $m_2$ ) is approximately decomposed to the three terms for a distant observer along the  $z$ -axis in Figure 1:

$$V_{\text{RV}}(t) = V_{\text{Kep}}^{(0)}(t) + \delta V_{\text{Kep}}(t) + V_{\text{bin}}(t). \quad (1)$$

The first term in the right-hand-side of equation (1) corresponds to the unperturbed Keplerian motion of the star around the barycenter of the system:

$$V_{\text{Kep}}^{(0)}(t) = K_0 \sin I_{\text{out}} \cos[\nu_{\text{out}} t + f_{\text{out},0} + \omega_{\text{out}}], \quad (2)$$

$$K_0 \equiv \frac{m_1 + m_2}{m_1 + m_2 + m_*} a_{\text{out}} \nu_{\text{out}}, \quad (3)$$

where  $K_0$  is the semi-amplitude of the unperturbed Keplerian RV for an edge-on observer,  $\nu_{\text{out}}$  and  $\omega_{\text{out}}$  denote the mean motion and argument of pericenter of the outer star, and  $f_{\text{out},0}$  is the initial true anomaly of the star at  $t = 0$ . Since orbits in a triple system should have a non-vanishing eccentricity,  $\omega_{\text{out}}$  in the above expressions is well defined in general.

The second term is the lowest-order perturbation correction to the stellar Keplerian motion due to the inner binary:

$$\delta V_{\text{Kep}}(t) = K_1 \sin I_{\text{out}} \cos[\nu_{\text{out}} t + f_{\text{out},0} + \omega_{\text{out}}], \quad (4)$$

$$K_1 \equiv \frac{3}{4} K_0 \left( \frac{a_{\text{in}}}{a_{\text{out}}} \right)^2 \frac{m_1 m_2}{(m_1 + m_2)^2}. \quad (5)$$

Finally the third term is the RV variation of the star with roughly twice the orbital frequency of the inner binary:

$$V_{\text{bin}}(t) = -\frac{15}{16} K_{\text{bin}} \sin I_{\text{out}} \cos[(2\nu_{\text{in}} - 3\nu_{\text{out}})t + 2(f_{\text{in},0} + \omega_{\text{in}}) - 3(f_{\text{out},0} + \omega_{\text{out}})] \\ + \frac{3}{16} K_{\text{bin}} \sin I_{\text{out}} \cos[(2\nu_{\text{in}} - \nu_{\text{out}})t + 2(f_{\text{in},0} + \omega_{\text{in}}) - (f_{\text{out},0} + \omega_{\text{out}})], \quad (6)$$

$$K_{\text{bin}} \equiv \frac{m_1 m_2}{(m_1 + m_2)^2} \sqrt{\frac{m_1 + m_2 + m_*}{m_1 + m_2}} \left( \frac{a_{\text{in}}}{a_{\text{out}}} \right)^{7/2} K_0, \quad (7)$$

where  $K_{\text{bin}}$  is the characteristic semi-amplitude of the RV variation of our primary interest,  $\nu_{\text{in}}$  and  $\omega_{\text{in}}$  denote the mean motion and argument of pericenter of the inner binary, and  $f_{\text{in},0}$  is the initial true anomaly of the inner binary at  $t = 0$ . Equation (6) indicates that the RV variation indeed consists of two slightly different frequency modes around  $2\nu_{\text{in}}$ :

$$\nu_{-3} \equiv 2\nu_{\text{in}} - 3\nu_{\text{out}}, \quad (8)$$

$$\nu_{-1} \equiv 2\nu_{\text{in}} - \nu_{\text{out}}. \quad (9)$$

Since we are interested in the case of  $\nu_{\text{in}} \gg \nu_{\text{out}}$ , the above two modes may be degenerate unless the observational duration is sufficiently long, and the cadence is sufficiently high.

In the case of  $m_1 = m_2 \gg m_*$ , the ratio of the above three semi-amplitudes is simplified as

$$K_0 : K_1 : K_{\text{bin}} = 1 : \frac{3}{16} \left( \frac{a_{\text{in}}}{a_{\text{out}}} \right)^2 : \frac{1}{4} \left( \frac{a_{\text{in}}}{a_{\text{out}}} \right)^{7/2}. \quad (10)$$

We note also that the above expressions for a prograde triple can be applied to a retrograde triple of the same orbits if  $\nu_{\text{in}}$ ,  $\omega_{\text{in}}$ , and  $f_{\text{in},0}$  are replaced by  $-\nu_{\text{in}}$ ,  $-\omega_{\text{in}}$ , and  $-f_{\text{in},0}$ , respectively. In the retrograde triple, therefore, we define the mean motions of the two modes:

$$\nu_{+3} \equiv 2\nu_{\text{in}} + 3\nu_{\text{out}}, \quad (11)$$

$$\nu_{+1} \equiv 2\nu_{\text{in}} + \nu_{\text{out}}. \quad (12)$$

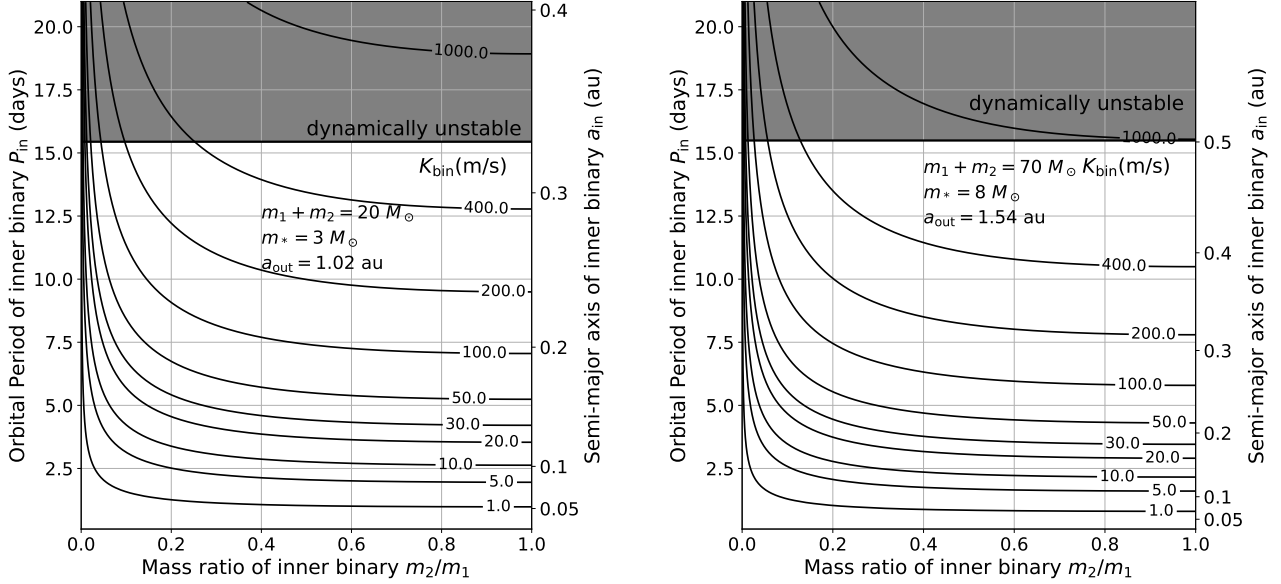


**Figure 2.** Contours of semi-amplitude of RV variations  $K_{\text{bin}}$  expected from an inner BBH in the LB-1 system. Each contour curve is labeled by the value of  $K_{\text{bin}}$  in units of m/s. The gray areas indicate the dynamically unstable region for a coplanar case in Newtonian theory; see inequality (14).

As in Paper I, the orbital period and mass ratio of a possible inner BBH in the LB-1 system are constrained from its dynamical stability. First note that the mass function of the LB-1 system (Liu et al. 2019) is observationally estimated to be

$$\frac{m_{12}^3 \sin^3 I_{\text{out}}}{(m_{12} + m_*)^2} = \frac{P_{\text{out}} K_{\text{out}}^3}{2\pi \mathcal{G}} (1 - e_{\text{out}}^2)^{3/2} = 1.02 \pm 0.05 M_{\odot}, \quad (13)$$

where  $\mathcal{G}$  is Newton's gravitational constant,  $I_{\text{out}}$  is the inclination of the stellar orbit with respect to our line of sight, and  $K_{\text{out}}$  is the observed semi-amplitude of the radial velocity. We denote the mass of the unseen companion of the star by  $m_{12}$ , which should be interpreted as  $m_1 + m_2$  if the LB-1 is a triple system hosting an inner binary.

We consider two specific examples following the original claims for the LB-1 according to Abdul-Masih et al. (2020); El-Badry & Quataert (2020); Liu et al. (2019):  $(m_{12}, m_*, I_{\text{out}}) = (20M_{\odot}, 3M_{\odot}, 24^\circ)$  and  $(70M_{\odot}, 8M_{\odot}, 15^\circ)$ , instead of the more recent estimate of  $(7M_{\odot}, 1.5M_{\odot}, 39^\circ)$  by Shenar et al. (2020). The former corresponds to our fiducial model in this paper, but we also consider the latter just for comparison because it corresponds roughly to a range of several BBHs detected by LIGO. We fix  $e_{\text{out}} = 0.03$  and  $P_{\text{out}} = 78.9$  days (Liu et al. 2019) for the outer star. These values are basically the same as those in Shenar et al. (2020);  $e_{\text{out}} = 0.0036 \pm 0.0021$  and  $P_{\text{out}} = 78.7999 \pm 0.0097$ .

Figure 2 plots a contour of  $K_{\text{bin}}$ , equation (7), on the  $m_2/m_1 - P_{\text{in}} (\equiv 2\pi/\nu_{\text{in}})$  plane, where we assume coplanar and near-circular orbits. The upper shaded regions are excluded from the dynamical instability condition for the three-body system. The noncoplanarity between the inner and outer orbits generally weakens the constraint for the coplanar case, and the instability condition is approximately given as (Mardling & Aarseth 1999, 2001; Aarseth & Mardling 2001; Toonen et al. 2016)

$$\frac{a_{\text{in}}}{a_{\text{out}}} > \frac{1 - e_{\text{out}}}{2.8(1 - 0.3i_{\text{mut}}/\pi)} \left( \frac{(1 + m_*/m_{12})(1 + e_{\text{out}})}{\sqrt{1 - e_{\text{out}}}} \right)^{-\frac{2}{5}}. \quad (14)$$

**Table 1.** Simulation models

model	$I_{\text{out}}$ (deg)	$I_{\text{in}}$ (deg)	$i_{\text{mut}}$ (deg)	$m_1$ ( $M_{\odot}$ )	$m_2$ ( $M_{\odot}$ )	$e_{\text{in}}$
P1010	90	90	0	10	10	$10^{-5}$
PE1010	90	90	0	10	10	0.2
R1010	90	270	180	10	10	$10^{-5}$
O1010	0	90	90	10	10	$10^{-5}$
I1010	0	45	45	10	10	$10^{-5}$
P0218	90	90	0	18	2	$10^{-5}$
PE0218	90	90	0	18	2	0.2
R0218	90	270	180	18	2	$10^{-5}$
O0218	0	90	90	18	2	$10^{-5}$
I0218	0	45	45	18	2	$10^{-5}$

NOTE—P, PE, R, O and I indicate prograde, prograde eccentric, retrograde, orthogonal and inclined orbits.

In the above inequality, the factor  $(1 - 0.3i_{\text{mut}}/\pi)$  is empirically added by [Aarseth & Mardling \(2001\)](#) so as to reproduce the earlier result by [Harrington \(1972\)](#). Figure 2 implies that an inner BBH of an orbital period between a few days and a couple of weeks is stable and has a potentially detectable RV variation amplitude. Thus, we adopt  $P_{\text{in}} = 10$  days in the rest of the paper. Note that this choice satisfies the empirical limit  $P_{\text{out}}/P_{\text{in}} \gtrsim 5$  for stellar triple systems listed in [Tokovinin \(2008\)](#).

### 3. RADIAL-VELOCITY VARIATION INDUCED BY AN INNER BINARY

#### 3.1. Simulation models and method for removing the quasi-Keplerian component from the radial velocity

As in Paper I, we perform N-body simulations for a set of triple configurations (Table 1), using the public N-body package **REBOUND** ([Rein & Liu 2012](#)). While our analysis in this paper is based on purely Newtonian gravity, we made sure that the correction due to general relativity (GR) does not change the conclusions here by repeating a set of runs using **REBOUNDx** ([Tamayo et al. 2020](#)), the extended package of **REBOUND**, with GR effects `gr_full` ([Newhall et al. 1983](#)); see section 4 below.

The initial conditions of the simulations are summarized in Table 2. For the simulations, we only consider the case  $(m_{12}, m_*) = (20M_{\odot}, 3M_{\odot})$  because the results are basically scalable for different mass regimes. We use **WHFast** integrator ([Rein & Tamayo 2015](#)) with a time step of  $10^{-6}$  yr/ $2\pi$ . We run each model and output the snapshots every 0.1 day over  $0 < t < 1000P_{\text{out}}^{(0)}$ , with  $P_{\text{out}}^{(0)} = 78.9$  days being the input orbital period of the outer star. We confirmed that all of the systems remain gravitationally bound and stable at least within  $1000P_{\text{out}}^{(0)}$ .

As we discussed in Paper I, all of the orbital parameters in the present simulation runs are time dependent, and the information for the inner BBH imprinted in the RV variations can be reproduced only when if the quasi-Keplerian RV component is properly extracted. While equation (1) provides a reasonably good approximation, it does not incorporate the back-reaction from the outer star, and cannot be directly applied to estimate the quasi-Keplerian RV component. Thus, we first fit the total RV using the public code **RadVel** ([Fulton et al. 2018](#)) to extract the quasi-Keplerian RV component.



**Table 2.** Initial values of the common parameters

parameter	initial value
orbital period $P_{\text{out}}$	78.9 days
orbital period $P_{\text{in}}$	10.0 days
eccentricity $e_{\text{out}}$	0.03
argument of pericenter $\omega_{\text{in}}$	0 deg
argument of pericenter $\omega_{\text{out}}$	0 deg
longitude of ascending node $\Omega_{\text{in}}$	0 deg
longitude of ascending node $\Omega_{\text{out}}$	0 deg
true anomaly $f_{\text{in}}$	30 deg
true anomaly $f_{\text{out}}$	120 deg
tertiary mass $m_*$	$3 M_{\odot}$
inner binary mass $m_1 + m_2$	$20 M_{\odot}$

Then, we compute the residual RV variations due to the inner BBH, perform the Lomb-Scargle (LS) periodogram analysis, and compare with the approximate analytic results.

Consider the prograde, coplanar and circular case with  $m_1 = m_2 = 10M_{\odot}$  (P1010 in Table 1). We use the initial orbital period of the star,  $P_{\text{out}}^{(0)} (= 78.9 \text{ days})$ , to normalize the time  $t$ . Strictly speaking, the initial conditions of the simulations (Table 2) are not dynamically consistent for the triple system. Thus we examine the evolution of the systems at  $t \geq 100P_{\text{out}}^{(0)}$  when the possible initial transient behavior goes away.

Figure 3 plots the total RV of P1010 for  $100 < t/P_{\text{out}}^{(0)} < 120$ . The black dots and magenta dashed line indicate the simulation output and an analytic approximation by [Morais & Correia \(2008\)](#). For the latter, we evaluate the orbital variables at  $t = 100P_{\text{out}}^{(0)}$ , and substitute those instantaneous values in equation (1). As expected, Figure 3 shows that the the total RV is dominated by the Keplerian motion, but the corresponding instantaneous period  $P_{\text{out}}(t)$  from simulations is clearly smaller than  $P_{\text{out}}^{(0)}$ . Note that the orbital period evaluated with the instantaneous orbital elements at  $t = 100P_{\text{out}}^{(0)}$  does not differ much from  $P_{\text{out}}^{(0)}$ .

Therefore, we use a public code [RadVel \(Fulton et al. 2018\)](#), and estimate the value of the quasi-Keplerian period  $P_{\text{out}}(t_n \equiv nP_{\text{out}}^{(0)})$  by fitting the total RV over  $nP_{\text{out}}^{(0)} < t < (n+1)P_{\text{out}}^{(0)}$  where  $n(\geq 100)$  is an integer. Figure 4 shows the resulting best-fit values of  $P_{\text{out}}(t_n)$  over  $100 \leq n < 200$  for P1010, R1010, and PE1010.

Equations (1) – (7) on the basis of a perturbation approximation by [Morais & Correia \(2008\)](#) assume that both the outer mean motion  $\nu_{\text{out}}$  and the argument of pericenter  $\omega_{\text{out}}$  are constant. In reality, however, they are dependent on time due to the perturbation from the inner binary. Let us consider the following expansions:

$$\nu_{\text{out}}(t) = \nu_{\text{out}}^{(0)} + \delta\nu_{\text{out}}(t), \quad (15)$$

$$\omega_{\text{out}}(t) = \omega_{\text{out}}^{(0)} + \delta\omega_{\text{out}}(t), \quad (16)$$

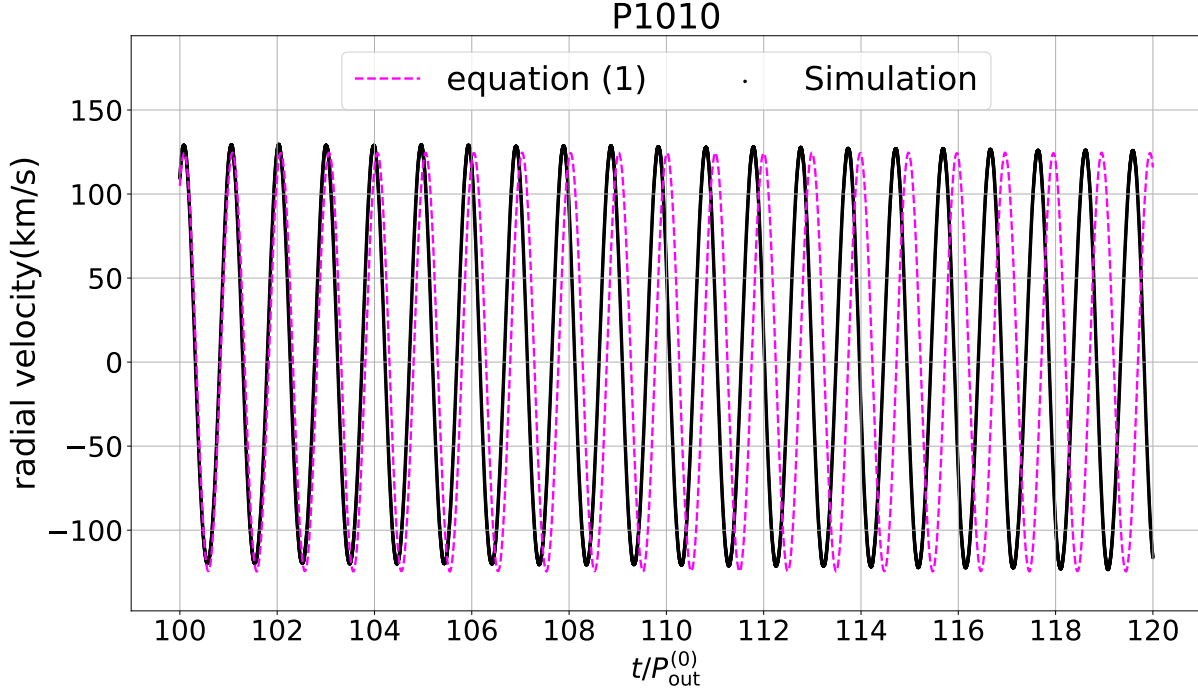


**Figure 3.** Radial velocity(P1010) with 0.1 day cadence. The black points and magenta dashed line denote the simulated RV data and RV approximate formula (equation (1)) evaluated at  $t = 100P_{\text{out}}^{(0)}$ , respectively.

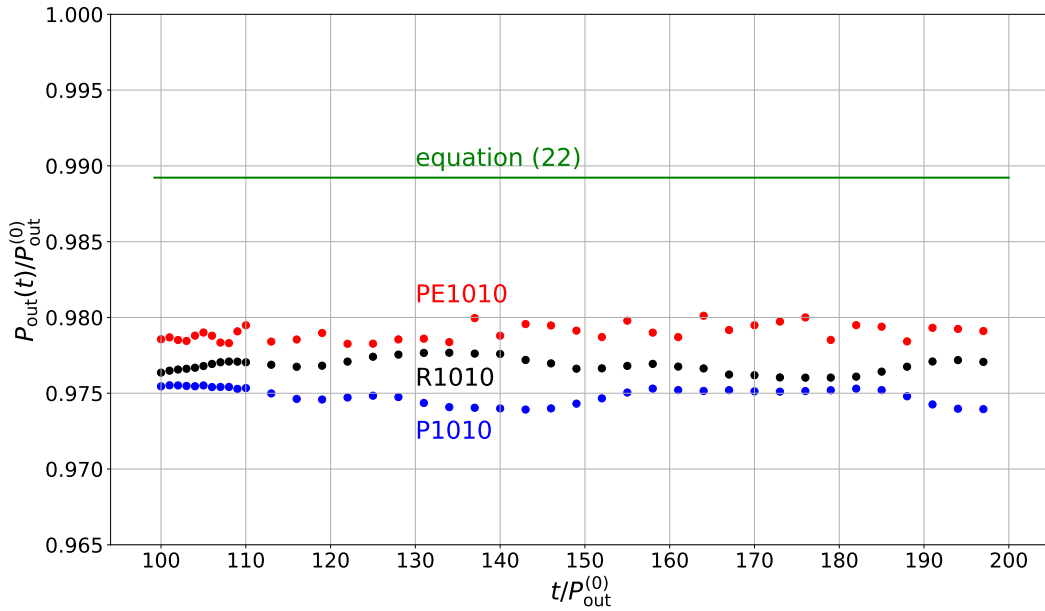


**Figure 4.** Best-fit values of  $P_{\text{out}}(t_n \equiv nP_{\text{out}}^{(0)})$  for coplanar systems. They are estimated with RadVel using the 0.1 day cadence simulated RV data over  $nP_{\text{out}}^{(0)} < t < (n+1)P_{\text{out}}^{(0)}$  for  $100 \leq n < 200$ ; P1010 (blue), R1010 (black), and PE1010 (red). The solid green line indicates the analytic prediction that incorporates the average time derivative of the argument of pericenter  $\omega_{\text{out}}(t)$  (see equation (22)).



where

$$\nu_{\text{out}}^{(0)} \equiv \sqrt{\frac{\mathcal{G}(m_{12} + m_*)}{(a_{\text{out}}^{(0)})^3}} \quad (17)$$

is the mean motion expected for the two-body system.

Figure 5 plots  $\omega_{\text{out}}(t)$  from the 0.1 day cadence output of our REBOUND run for P1010, PE1010, R1010, and P0218. It is clearly visible that  $\omega_{\text{out}}(t)$  exhibits periodic modulations with frequency roughly corresponding to  $\nu_{\text{out}}$  and  $\nu_{\text{in}}$ , in addition to the monotonic increase with  $t$ . In order to remove the oscillation components, we compute the time average of  $\omega_{\text{out}}$  over  $nP_{\text{out}}^{(0)} < t < (n+1)P_{\text{out}}^{(0)}$  using RadVel as described in the above, and plot the best-fit values  $\langle \omega_{\text{out}} \rangle$  in solid circles at  $t = t_n$ .

The time derivative of  $\omega_{\text{out}}$  is given by (see Appendix A for details)

$$\frac{\dot{\omega}_{\text{out}}}{2\pi} = \frac{3}{4} \frac{1}{P_{\text{out}}} \left( \frac{a_{\text{in}}}{a_{\text{out}}} \right)^2 \left( \sqrt{\frac{m_2}{m_1}} + \sqrt{\frac{m_1}{m_2}} \right)^{-2} \frac{1}{(1 - e_{\text{out}}^2)^2}, \quad (18)$$

for a coplanar triple system with  $e_{\text{in}}^2 \ll 1$ . The slope of the dashed lines in Figure 5 corresponds to the prediction of equation (18) evaluating with input values of orbital parameters (see Tables 1 and 2), which reproduces the behavior of  $\langle \omega_{\text{out}} \rangle(t)$  very well. This good agreement indicates that  $\delta\omega_{\text{out}}(t)$  in equation (16) averaged over  $P_{\text{out}}^{(0)}$  is well approximated by  $\dot{\omega}_{\text{out}}t$  with equation (18).

Thus, the pericenter shift itself provides an independent signature of the presence of the inner binary. Indeed, this is why a hypothetical planet Vulcan was proposed by Le Verrier (1859) to explain the anomalous perihelion shift of Mercury in Newton's theory before general relativity was discovered by Einstein (1915).

This implies that the sinusoidal term in the right-hand side of equations (2) and (4) can be written, to its lowest order, as

$$\cos[\nu_{\text{out}}(t)t + \omega_{\text{out}}(t) + f_{\text{out},0}] \approx \cos[(\nu_{\text{out}}^{(0)} + \delta\nu_{\text{out}}(0) + \dot{\omega}_{\text{out}})t + \omega_{\text{out}}^{(0)} + f_{\text{out},0}]. \quad (19)$$

Equation (19) suggests that  $P_{\text{out}}(t)$  averaged over  $P_{\text{out}}^{(0)}$  should be

$$P_{\text{out}}(t) = \frac{2\pi}{\nu_{\text{out}}^{(0)} + \delta\nu_{\text{out}}(0) + \dot{\omega}_{\text{out}}}. \quad (20)$$

In the case of a coplanar and circular triple with the equal-mass inner binary, equation (18) reduces to

$$\frac{\dot{\omega}_{\text{out}}}{2\pi} \approx \frac{0.011}{P_{\text{out}}} \left( \frac{P_{\text{in}}}{10 \text{ days}} \right)^{4/3} \left( \frac{P_{\text{out}}}{78.9 \text{ days}} \right)^{-4/3} \left( \frac{m_1 + m_2}{20M_{\odot}} \right)^{2/3} \left( \frac{m_1 + m_2 + m_*}{23M_{\odot}} \right)^{-2/3}. \quad (21)$$

Therefore, if  $\delta\nu_{\text{out}}(0)$  can be neglected, equation (20) predicts that

$$\frac{P_{\text{out}}(t)}{P_{\text{out}}^{(0)}} \approx 1 - \frac{\dot{\omega}_{\text{out}}P_{\text{out}}^{(0)}}{2\pi} \approx 0.989. \quad (22)$$

As plotted in Figure 4, however, equation (22) accounts for approximately one-half of the systematic decrease of the simulation results, and not entirely. This may indicate that  $\delta\nu_{\text{out}}(0)$  cannot be

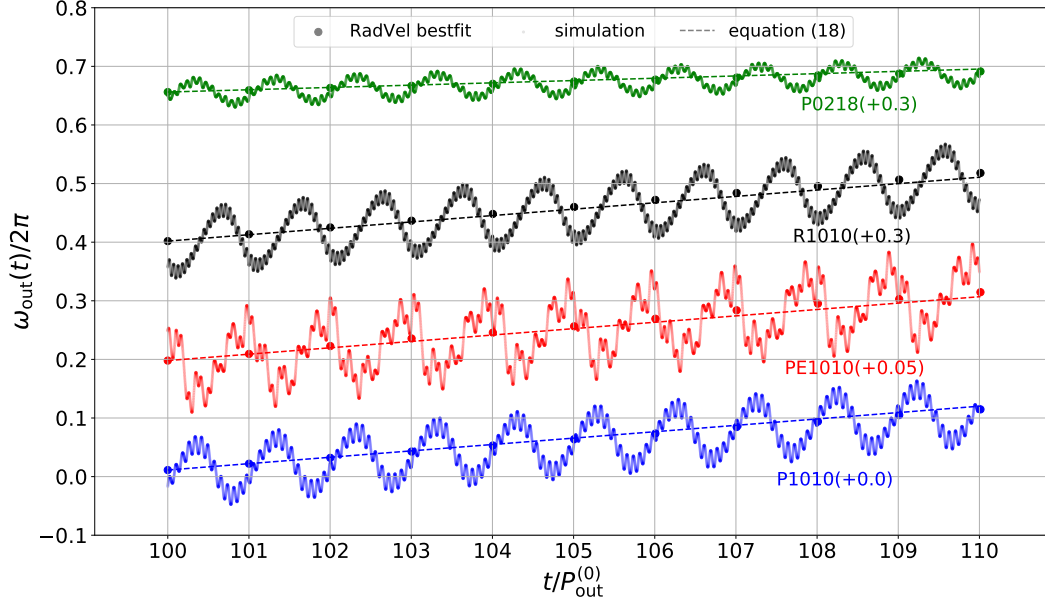


**Figure 5.** Best-fit values of  $\omega_{\text{out}}(t)$  for P1010, PE1010, R1010 and P0218. Each best-fit value is determined with RadVel from simulation data using their 0.1 day cadence outputs over  $1P_{\text{out}}^{(0)}$  starting at  $t$ . The dashed line is calculated using the analytic approximate formula of  $\dot{\omega}_{\text{out}}$  in equation (18). For clarity, the data are translated in the  $y$  direction with the offset value indicated in parentheses.

neglected. Indeed, a different perturbation analysis of the current systems on the basis of the Lagrange planetary equation seems to be successful in reproducing the offset of  $P_{\text{out}}(t)/P_{\text{out}}^{(0)}$  shown in Figure 4 (Hayashi et al. 2019); unpublished but posted in arXiv.1905.07100v1.

In any case, our strategy is to empirically remove the quasi-Keplerian RV component by local fitting of the data, instead of using the analytical template. Thus the above offset of  $P_{\text{out}}(t)/P_{\text{out}}^{(0)}$  does not affect our procedure for extracting the RV variations due to the inner binary. To be more specific, we use the RV data of the simulation runs over  $100P_{\text{out}}^{(0)} < t < 101P_{\text{out}}^{(0)}$ . Then we estimate  $P_{\text{out}}(t_{100})$  with RadVel, and remove the corresponding Keplerian component from the data. We analyze the residual RV variations using the LS periodogram to search for the signal that is due to the inner binary. The choice of  $100P_{\text{out}}^{(0)} < t < 101P_{\text{out}}^{(0)}$  is arbitrary, and we made sure that our main conclusion below is not affected by the choice of the epoch at all.

### 3.2. Coplanar orbits

The residual RV variations after removing the empirically fitted Keplerian component are plotted in Figure 6 for the coplanar and near-circular cases. The top, middle, and bottom panels correspond to P1010 (prograde and equal-mass binary), R1010 (retrograde and equal-mass binary), and P0218 (prograde and unequal-mass binary), respectively.

The left panels indicate the RV variations of the simulation runs (dots) in the time domain every 0.1 days over  $100P_{\text{out}}^{(0)} < t < 101P_{\text{out}}^{(0)}$ . For comparison, magenta curves show the analytic approximation:

$$V_{\text{bin},i}(t) = -\frac{15}{16}K_{\text{bin}}^{(i)} \cos[\nu_{\mp 3}^{(i)}t + 2(f_{\text{in},0}^{(i)} + \omega_{\text{in}}^{(i)}) \mp 3(f_{\text{out},0}^{(i)} + \omega_{\text{out}}^{(i)})]$$

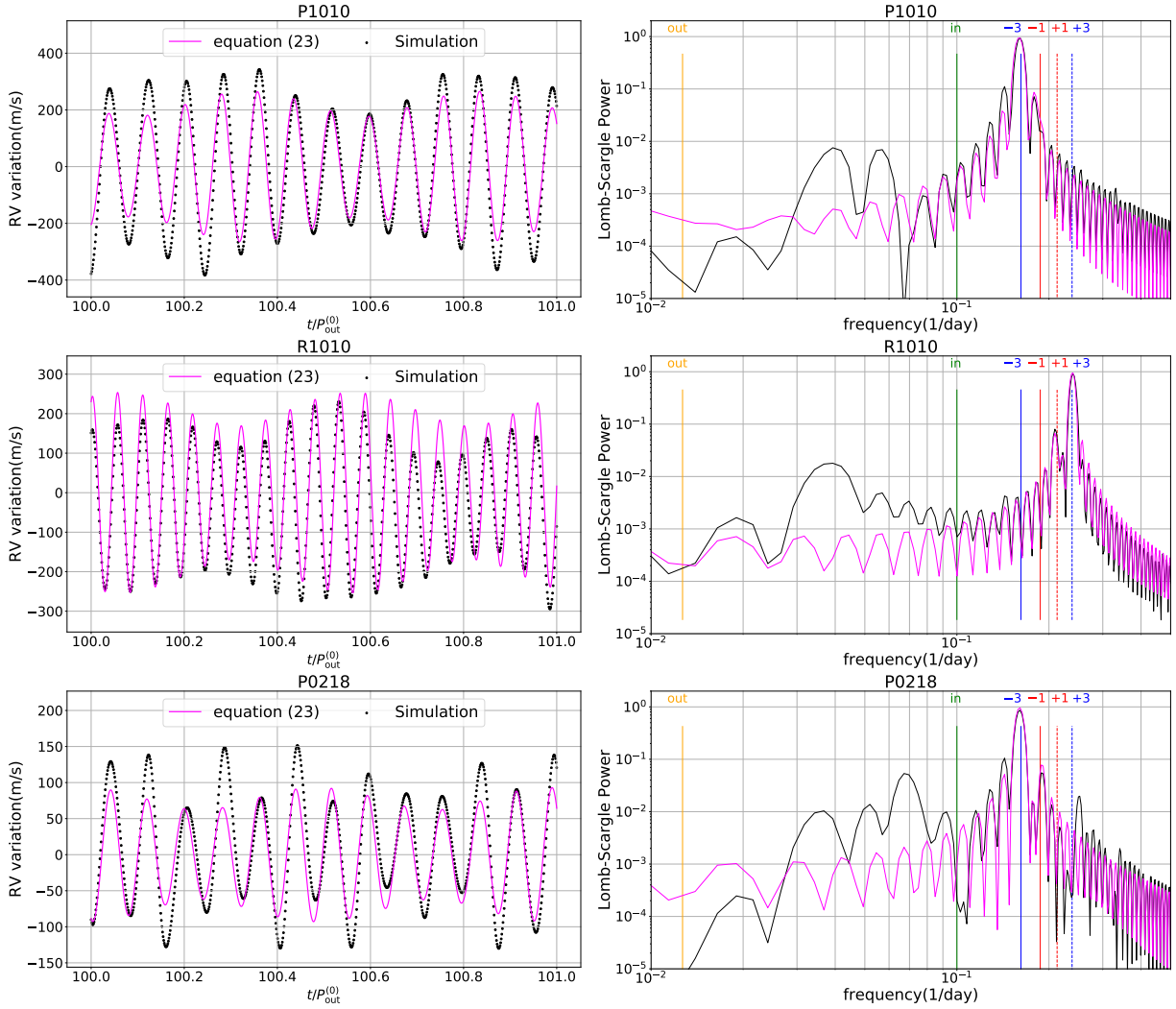


**Figure 6.** RV variations for P1010, R1010, and P0218 with 0.1 day cadence: time series (left) and LS periodograms (right). The black points indicate the simulated RV variation determined with RadVel. The magenta lines show the approximate prediction for the RV variation, equation (23). In the right panels, the locations of the frequencies at  $\nu_{\text{out}}^{(0)}$ ,  $\nu_{\text{in}}^{(0)}$ ,  $\nu_{-3}^{(0)}$ ,  $\nu_{-1}^{(0)}$ ,  $\nu_{+1}^{(0)}$ , and  $\nu_{+3}^{(0)}$  are indicated by vertical lines labeled by out, in, -3, -1, +1, +3, respectively.

$$+\frac{3}{16}K_{\text{bin}}^{(i)} \cos[\nu_{\mp 1}^{(i)} t + 2(f_{\text{in},0}^{(i)} + \omega_{\text{in}}^{(i)}) \mp (f_{\text{out},0}^{(i)} + \omega_{\text{out}}^{(i)})], \quad (23)$$

$$\nu_{\mp 3}^{(i)} \equiv 2\nu_{\text{in}}^{(i)} \mp 3\nu_{\text{out}}^{(i)}, \quad (24)$$

$$\nu_{\mp 1}^{(i)} \equiv 2\nu_{\text{in}}^{(i)} \mp \nu_{\text{out}}^{(i)}, \quad (25)$$

where the minus and plus signs are for prograde and retrograde orbits, respectively. We introduce the superscript (i) so as to indicate instantaneous orbital elements evaluated at  $t_i = 100P_{\text{out}}^{(0)}$ . We evaluate equation (1) using the instantaneous orbital elements at  $t_i$  rather than their input values (Table 2). This is necessary to accurately estimate the phases  $f_{\text{in},0}^{(i)} + \omega_{\text{in}}^{(i)}$  and  $f_{\text{out},0}^{(i)} + \omega_{\text{out}}^{(i)}$  in order for the numerical results to reproduce the approximate formula.

Equation (23) reproduces the amplitudes of the RV variations from the simulations (left panels in Figure 6) reasonably well. Note that the simulated RV variations are dependent on the empirically removed quasi-Keplerian component, while equation (23) is the lowest-order perturbation approximation neglecting the back-reaction of the outer star on the inner orbit. Therefore, the discrepancy between the two should not be regarded as serious.

Nevertheless, the corresponding LS periodograms (right panels in Figure 6) clearly detect the presence of the periodic components that are due to the inner binary, especially at the frequencies of  $\nu_{-3}^{(0)}$  and  $\nu_{+3}^{(0)}$  for prograde and retrograde orbits, respectively. Furthermore, the lower-amplitude peak at the accompanying frequency ( $\nu_{-1}^{(0)}$  or  $\nu_{+1}^{(0)}$ ) can imply in principle whether the inner and outer orbits are prograde or retrograde. The agreement between the simulations and predictions is degraded for frequencies less than  $\nu_{\text{in}}^{(0)}$ , which likely results from the uncertainty of the empirical removal of the underlying quasi-Keplerian RV component, as mentioned in the above. The LS periodograms prove, however, that the frequency modes at  $\nu_{\pm 3}^{(0)}$  and  $\nu_{\pm 1}^{(0)}$  are fairly robust against the removal procedure.

Incidentally, the agreement between the simulation and predictions seems worse for the unequal-mass binary case (P0218). This is thought to come from the higher-order perturbation effect; the larger mass difference of the binary enhances the octupole (e.g. Mardling 2013), which is neglected in the approximation by Morais & Correia (2008).

### 3.3. Effect of the eccentricity of the inner binary on the stellar radial velocity variation

Both  $e_{\text{in}}$  and  $e_{\text{out}}$ , the eccentricities of the inner and outer orbits, sensitively change the RV variations as shown in Paper I. The outer stellar orbit could be very eccentric, but we neglect it in the present paper because  $e_{\text{out}}$  is estimated to be 0.03 for the LB-1 system (Liu et al. 2019). On the other hand,  $e_{\text{in}}$  is expected to be not so large for BBHs that we are primarily interested in, because of the circularization due to the emission of the gravitational wave, especially for those with a short orbital period. Therefore, we focus on the effect of relatively small  $e_{\text{in}}$  on the RV variation of the tertiary star in coplanar triple systems.

Morais & Correia (2011) have derived an analytic approximation for the RV variation in a coplanar eccentric triple, to the lower order of  $e_{\text{in}}$  and  $e_{\text{out}}$ :

$$V_{\text{RV}}(t) = V_{\text{Kep}}^{(0)}(t) + \delta V_{\text{Kep}}(t) + V_{\text{bin}}(t), \quad (26)$$

where  $V_{\text{Kep}}^{(0)}(t)$  is the unperturbed Keplerian radial velocity, and  $\delta V_{\text{Kep}}(t)$  in a coplanar eccentric case is now written as

$$\delta V_{\text{Kep}}(t) = K_1 \sin I_{\text{out}} \cos(\nu_{\text{out}} t + \lambda_{\text{out},0}), \quad (27)$$

in terms of the initial mean longitude  $\lambda_{j,0}$ . The true anomaly  $f$  and argument of pericenter  $\omega$  can be expanded in terms of the small eccentricity  $e$  as

$$f + \omega = \lambda + 2e \sin(\lambda - \omega) + \mathcal{O}(e^2), \quad (28)$$

(e.g. Murray & Dermott 2000). Thus  $f + \omega$  is identical to  $\lambda$  for a circular case, and equation (4) reduces to equation (27). In an eccentric case, however, equation (28) is necessary to clarify the effect of the eccentricities in a perturbative manner.

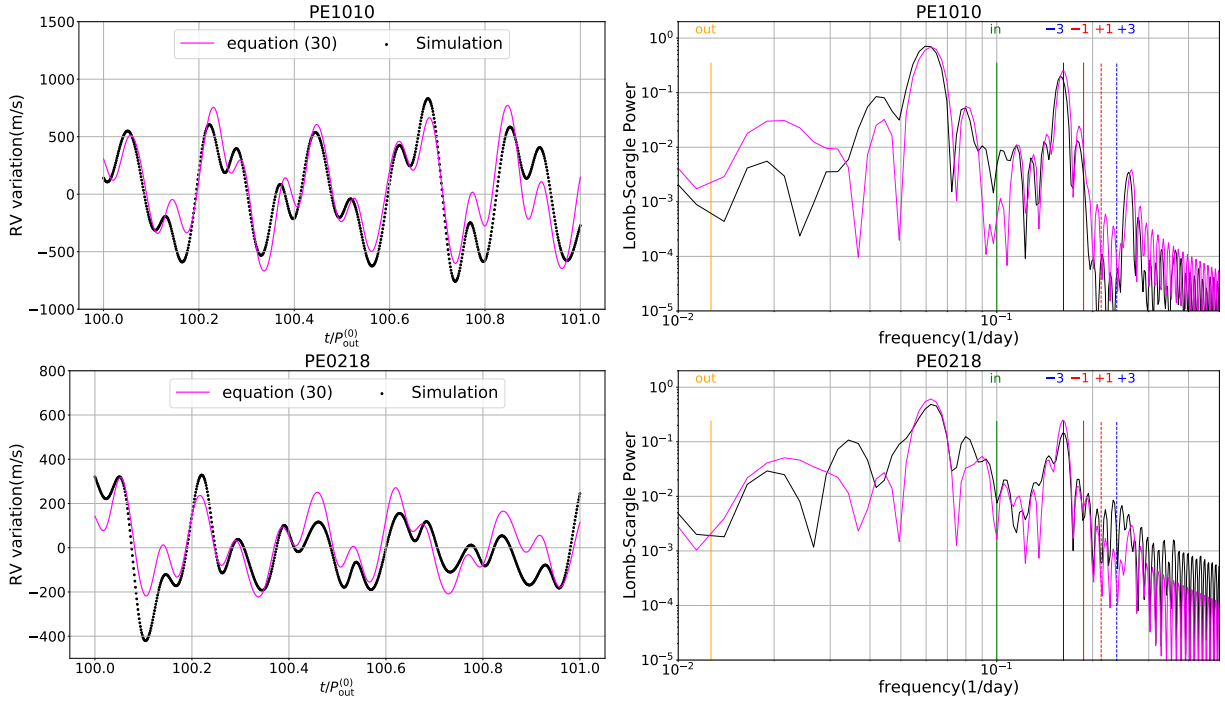


**Figure 7.** Same as Figure 6 but for PE1010 and PE0218. The magenta lines show the approximate formula (equation (30)) evaluated at  $t = 100P_{\text{out}}^{(0)}$ . The phase and constant offsets ( $\delta t, C$ ) are empirically determined to match the simulated residuals:  $(\delta t, C) = (+0.115P_{\text{out}}^{(0)}, -480.0)$  and  $(-0.27P_{\text{out}}^{(0)}, -430.0)$  for PE1010 and PE0218, respectively.

An analytic approximation for  $V_{\text{bin}}(t)$  in equation (26) is derived by [Morais & Correia \(2011\)](#), which is explicitly written as

$$\begin{aligned}
 V_{\text{bin}}^{\text{MC}}(t) = & \frac{3}{8} K_{\text{bin}} \sin I_{\text{out}} \times \left[ \frac{\nu_{\text{in}}}{2\nu_{\text{in}} - \nu_{\text{out}}} \cos[(2\nu_{\text{in}} - \nu_{\text{out}})t + 2\lambda_{\text{in},0} - \lambda_{\text{out},0}] \right. \\
 & - \frac{5\nu_{\text{in}}}{2\nu_{\text{in}} - 3\nu_{\text{out}}} \cos[(2\nu_{\text{in}} - 3\nu_{\text{out}})t + 2\lambda_{\text{in},0} - 3\lambda_{\text{out},0}] \\
 & + 15e_{\text{in}} \frac{\nu_{\text{in}}}{\nu_{\text{in}} - 3\nu_{\text{out}}} \cos[(\nu_{\text{in}} - 3\nu_{\text{out}})t + \lambda_{\text{in},0} - 3\lambda_{\text{out},0} + \varpi_{\text{in}}] \\
 & + e_{\text{in}} \frac{\nu_{\text{in}}}{3\nu_{\text{in}} - \nu_{\text{out}}} \cos[(3\nu_{\text{in}} - \nu_{\text{out}})t + 3\lambda_{\text{in},0} - \lambda_{\text{out},0} - \varpi_{\text{in}}] \\
 & - 5e_{\text{in}} \frac{\nu_{\text{in}}}{3\nu_{\text{in}} - 3\nu_{\text{out}}} \cos[(3\nu_{\text{in}} - 3\nu_{\text{out}})t + 3\lambda_{\text{in},0} - 3\lambda_{\text{out},0} - \varpi_{\text{in}}] \\
 & - 2e_{\text{in}} \frac{\nu_{\text{in}} + \nu_{\text{out}}}{\nu_{\text{in}} + \nu_{\text{out}}} \cos[(\nu_{\text{in}} + \nu_{\text{out}})t + \lambda_{\text{in},0} + \lambda_{\text{out},0} - \varpi_{\text{in}}] \\
 & - 3e_{\text{in}} \frac{\nu_{\text{in}}}{\nu_{\text{in}} - \nu_{\text{out}}} \cos[(\nu_{\text{in}} - \nu_{\text{out}})t + \lambda_{\text{in},0} - \lambda_{\text{out},0} + \varpi_{\text{in}}] \\
 & + 2e_{\text{in}} \frac{\nu_{\text{in}}}{\nu_{\text{in}} - \nu_{\text{out}}} \cos[(\nu_{\text{in}} - \nu_{\text{out}})t + \lambda_{\text{in},0} - \lambda_{\text{out},0} - \varpi_{\text{in}}] \\
 & + 6e_{\text{out}} \frac{\nu_{\text{in}}}{2\nu_{\text{out}}} \cos(2\nu_{\text{out}}t + 2\lambda_{\text{out},0} - \varpi_{\text{out}}) \\
 & + e_{\text{out}} \frac{\nu_{\text{in}}}{2\nu_{\text{in}}} \cos(2\nu_{\text{in}}t + 2\lambda_{\text{in},0} - \varpi_{\text{out}}) \\
 & \left. - 25e_{\text{out}} \frac{\nu_{\text{in}}}{2\nu_{\text{in}} - 4\nu_{\text{out}}} \cos[(2\nu_{\text{in}} - 4\nu_{\text{out}})t + 2\lambda_{\text{in},0} - 4\lambda_{\text{out},0} + \varpi_{\text{out}}] \right]
 \end{aligned}$$

$$\begin{aligned}
& +3 e_{\text{out}} \frac{\nu_{\text{in}}}{2\nu_{\text{in}} - 2\nu_{\text{out}}} \cos[(2\nu_{\text{in}} - 2\nu_{\text{out}})t + 2\lambda_{\text{in},0} - 2\lambda_{\text{out},0} + \varpi_{\text{out}}] \\
& +5 e_{\text{out}} \frac{\nu_{\text{in}}}{2\nu_{\text{in}} - 2\nu_{\text{out}}} \cos[(2\nu_{\text{in}} - 2\nu_{\text{out}})t + 2\lambda_{\text{in},0} - 2\lambda_{\text{out},0} - \varpi_{\text{out}}] \Big], \quad (29)
\end{aligned}$$

where  $\varpi_j = \omega_j + \Omega_j$ .

In reality, however, our simulation results have an uncertain offset relative to equation (29), and thus we model  $V_{\text{bin}}(t)$  as

$$V_{\text{bin}}(t) = V_{\text{bin}}^{\text{MC}}(t) - V_{\text{bin}}^{\text{MC}}(0) + V_0 + C. \quad (30)$$

In equation (30), we define  $V_0$  as the initial velocity of the RV variation, and  $C$  is an additional constant discussed below.

We first fit the simulation data using `RadVel` to obtain  $V_{\text{Kep}}^{(0)}(t) + \delta V_{\text{Kep}}(t)$  at  $t = t_i = 100P_{\text{out}}^{(0)}$ . Thus the residual RV variation from the simulation should correspond to  $V_{\text{bin}}(t)$ . We also evaluate all of the orbital elements and  $V_0$  at  $t_i$ , whose values are substituted into equation (29). Since the quasi-Keplerian component estimated with our fitting procedure involves a time average over an outer orbital period, the residual RV variation  $V_{\text{bin}}(t)$  from the simulation should inevitably have a time shift relative to equation (29). Thus we introduce an empirical time shift  $\delta t$  to match the analytical expression (29) and the simulation result. This matching simultaneously requires the additional velocity offset term  $C$ , which is introduced in equation (30).

Figure 7 shows the resulting plot of RV variations for PE1010 and PE0218. We find that the simulated RV variations in the left panel of Figure 7 agree well with the analytic approximation. Thus the presence of an inner binary can be detected even in a moderately eccentric coplanar system, as long as the observational data are sufficiently accurate to the level indicated in Figure 7.

### 3.4. *noncoplanar orbits*

Finally we examine how the noncoplanarity between the inner and outer orbits affects the RV variation. Since the general analysis of the noncoplanar case is not realistic, we focus on two specific initial configurations that we call inclined ( $i_{\text{mut}} = 45^\circ$ ; denoted by I) and orthogonal ( $i_{\text{mut}} = 90^\circ$ ; denoted by O).

The results are plotted in Figure 8, 9, 10, and 11 for I1010, O1010, I0218, and O0218, respectively. Each figure has eight panels; the top left panels display the trajectory of the direction of the angular momentum of the inner (red) and outer (blue) orbits. The numbers indicate  $t/P_{\text{out}}^{(0)}$ . The top right panels show the corresponding evolution of the mutual inclination ( $i_{\text{mut}}$ ), orbital inclinations ( $I_{\text{in}}$  and  $I_{\text{out}}$ ), and longitudes of the ascending nodes ( $\Omega_{\text{in}}$  and  $\Omega_{\text{out}}$ ). We plot the orbital parameters every one day output interval. The middle panels plot the RV variations and the corresponding LS periodograms viewed from the  $x$  and  $z$ -axes of the reference frame (Figure 1). The bottom panels plot the total RV curves, instead of the residual RV variations, viewed from the  $x$  and  $z$ -axes.

Consider first I1010, which has the mutual inclination of  $i_{\text{mut}} = 45^\circ$  initially. As shown in the top panels of Figure 8, the inner and outer orbits precess around the total angular momentum axis of the entire system in a periodic fashion. As described in Appendix A, this corresponds to the precession of the inner and outer orbits around the total angular momentum axis of the triple system. The period of  $\approx 65P_{\text{out}}^{(0)}$  is indeed well explained by the approximate formula in equation (A19). This roughly corresponds to the Kozai-Lidov oscillation timescale  $T_{\text{KL}}$  (Kozai 1962; Lidov 1962) (see Appendix A for details).

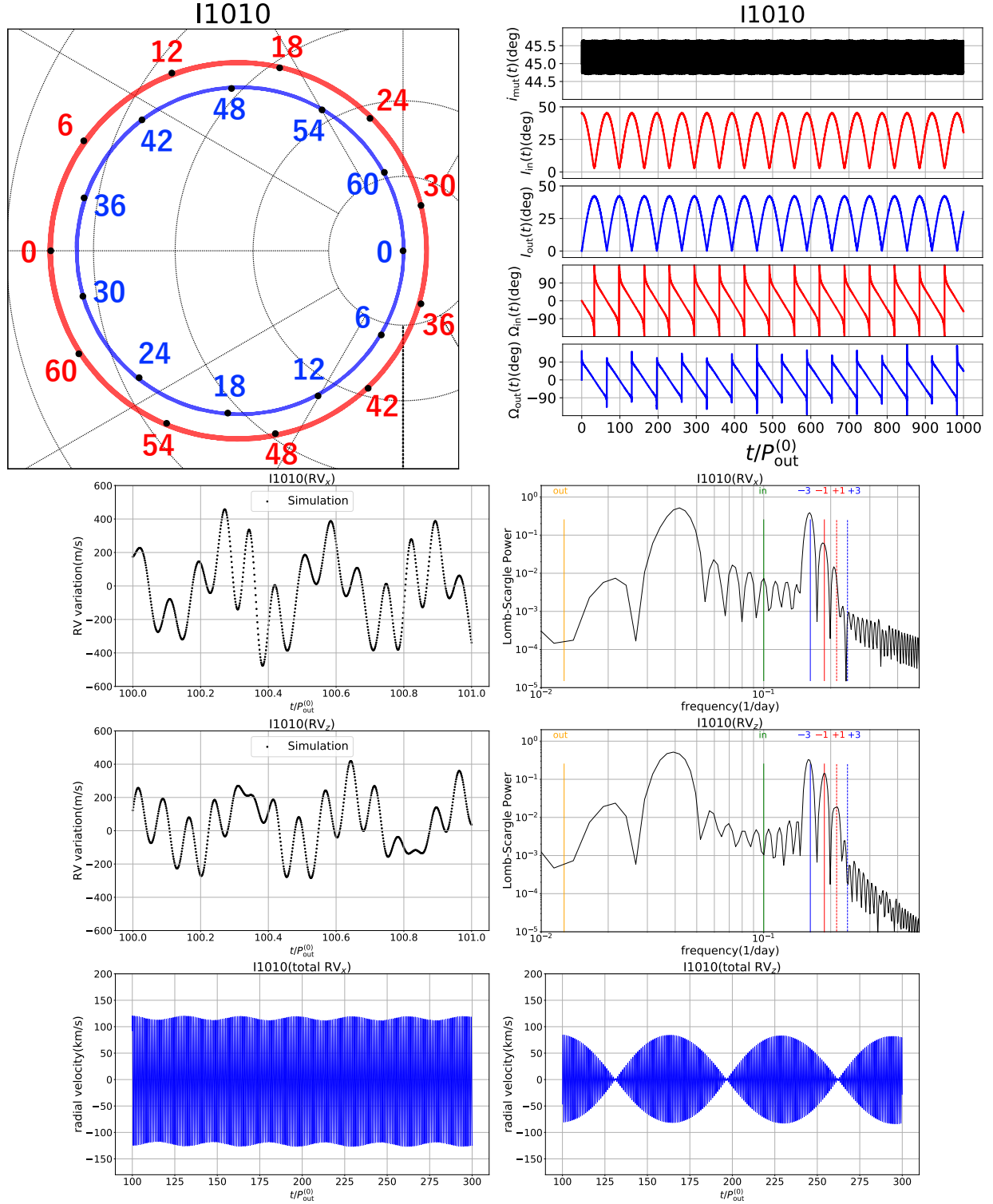


**Figure 8.** Behavior of the noncoplanar triple I1010: *Top*: evolution of orientation of the inner and outer orbits (in red and blue, respectively). The longitudinal and latitudinal lines in the left panel are drawn every 30 and 10 degrees, respectively. *Middle*: time series of RV variations along  $x$ ,  $z$  axes, and the corresponding LS periodograms. *Bottom*: total RV curves along the  $x$  (left) and  $z$  (right) axes.



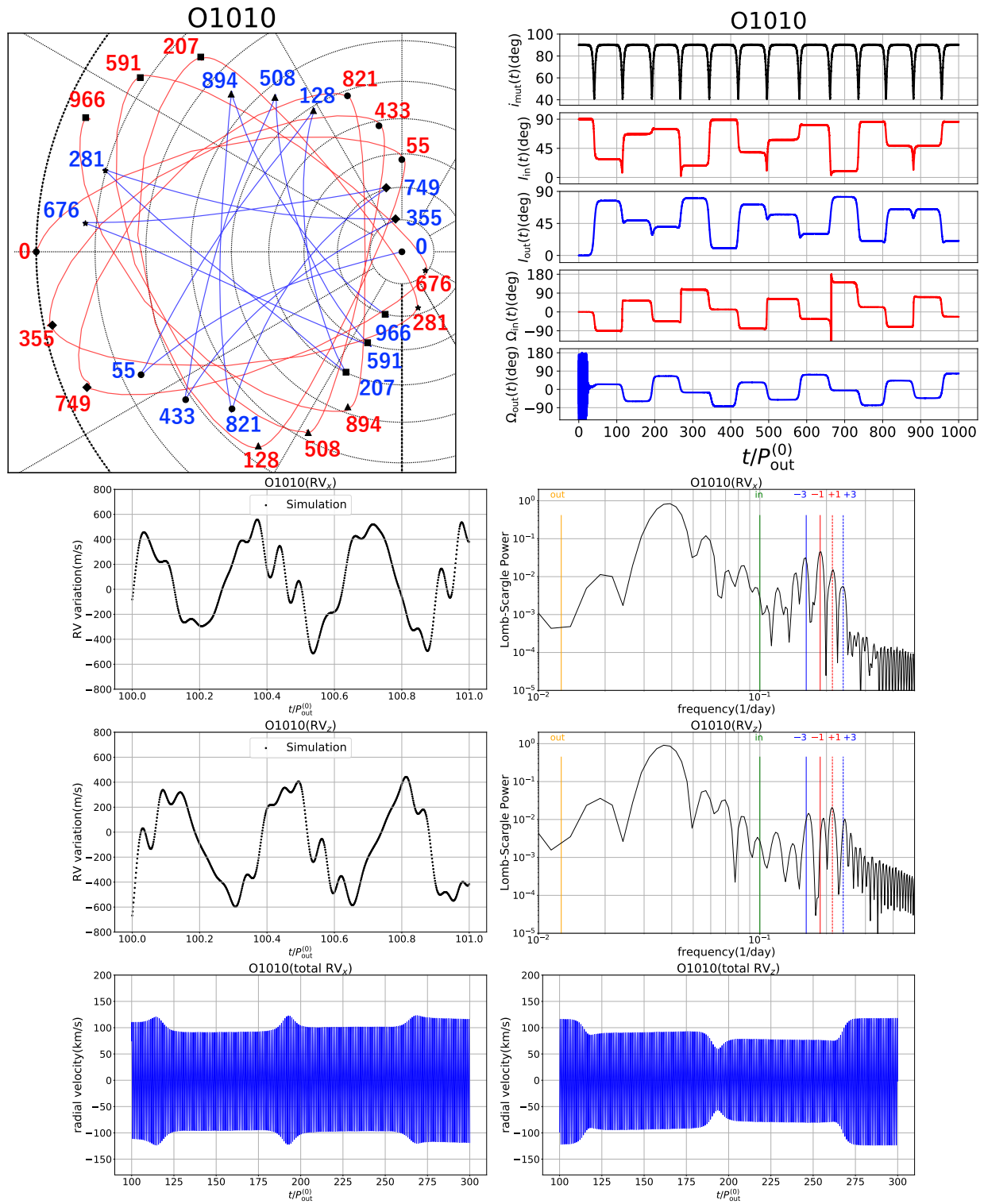


Figure 9. Same as Figure 8 but for O1010.

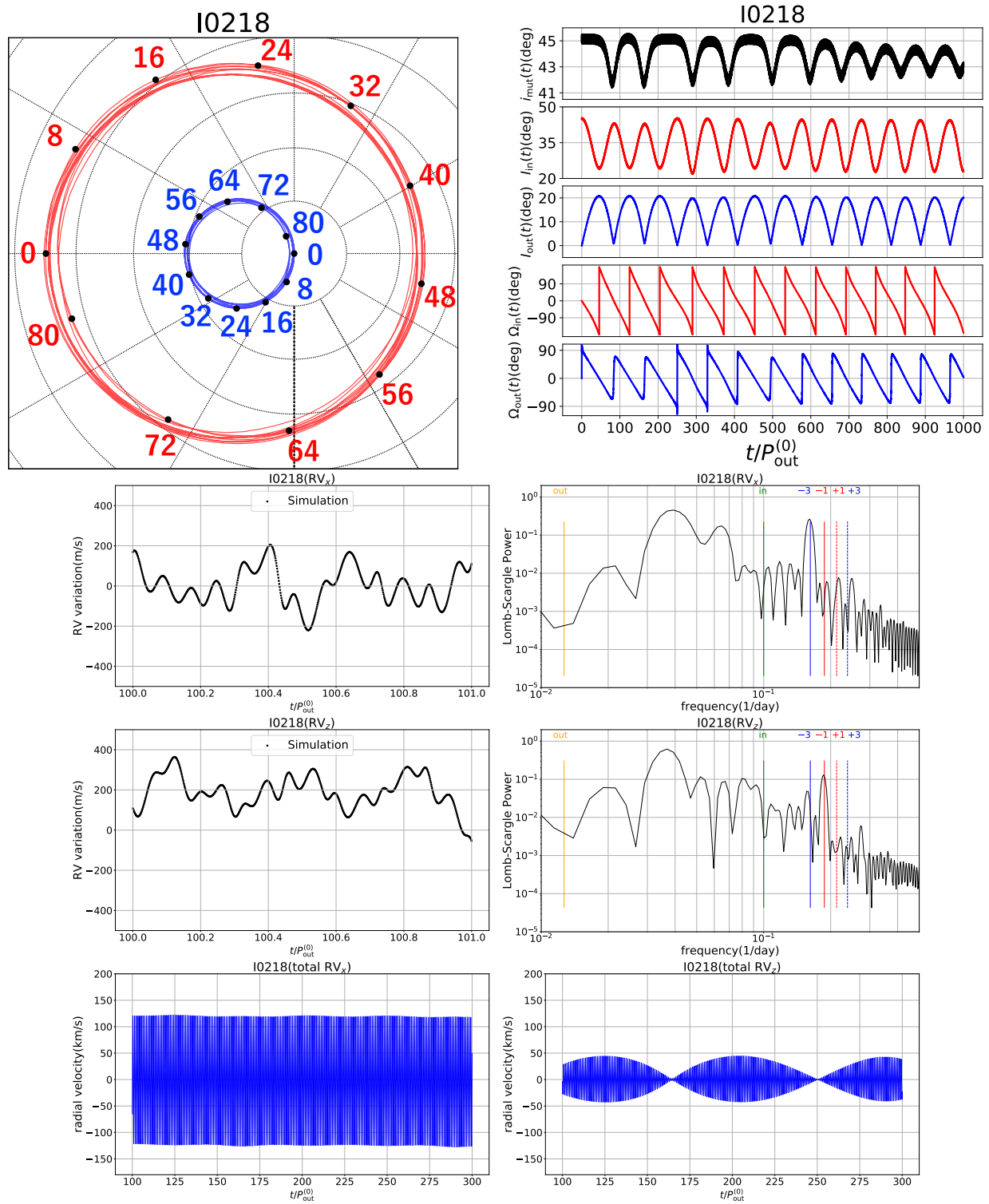


Figure 10. Same as Figure 8 but for I0218.

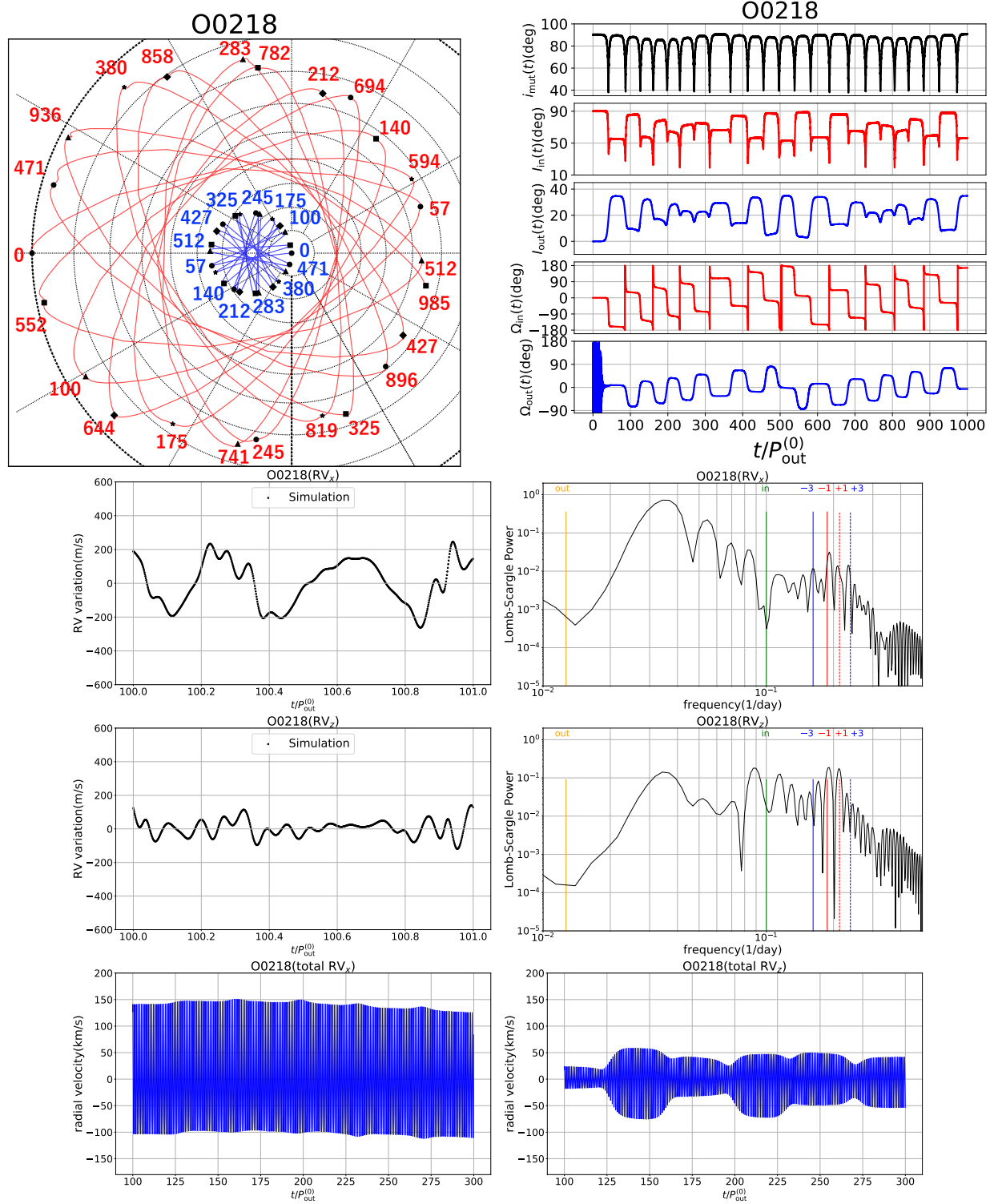


Figure 11. Same as Figure 8 but for O0218.

In this case, the evolution of the mutual inclination is fairly moderate, except for the precession, and the inner and outer orbits remain to be near-prograde with each other. Therefore, although the additional periodic terms are present in the RV variations, both the time series and the LS periodograms show clear modulations due to the inner binary at frequencies of  $\nu_{-3}$  and  $\nu_{-1}$ . Those trends should be generic for moderately inclined systems with  $i_{\text{mut}} < 45^\circ$ .

An interesting observable feature is the significant modulation of the Keplerian RV component over a timescale of  $T_{\text{KL}}$ , induced by the periodic variation of  $I_{\text{out}}$ . The bottom panels of Figure 8 show the RV amplitude modulation from nearly edge-on ( $x$ -axis) and face-on ( $z$ -axis) lines of sight. Since the time dependence of the total RV semi-amplitude is approximately given as

$$K_{\text{out}}(t) \approx K_0 \sin(I_{\text{out}}(t)) \approx K_0 \sin(I_{\text{out}}(t_0)) + K_0 \dot{I}_{\text{out}}(t_0) \cos(I_{\text{out}}(t_0))(t - t_0) + \mathcal{O}((t - t_0)^2), \quad (31)$$

large variations are expected especially for a nearly face-on (i.e.  $I_{\text{out}}(t_0) \approx 0^\circ$ ) case.

If the mutual inclination of the two orbits is much larger, the orbital orientations exhibit substantial dynamical evolution. This is illustrated in Figure 9 for the initially orthogonal orbits. In this case, the Kozai-Lidov oscillation (Kozai 1962; Lidov 1962) plays an important role in the evolution of inclinations themselves. Since the precession period given by equation (A19) is inversely proportional to  $\cos i_{\text{mut}}$ , the system stays for a long time at highly inclined states of  $i_{\text{mut}} \approx \pi/2$ . Gradually then, the inner eccentricity is extremely enhanced by the KL oscillation, and  $i_{\text{mut}}$  decreases rapidly. This behavior explains the drastic modulation on the semi-amplitude of RV as shown in the bottom panels of Figure 9.

Figure 8 implies that the directions of the angular momentum vectors in the initially inclined orbits (I1010) evolve in a fairly periodic and regular fashion. This is in marked contrast to the case of the initially orthogonal orbits; see the top left panel of Figure 9. The trajectories of the orientations of the inner and outer orbits for O1010 in the top left panel of Figure 9 seem to evolve in an irregular fashion. They first stay at the initial location represented by the filled circles labeled with 0 (blue and red for outer and inner orbits, respectively) until  $t \approx 30P_{\text{out}}^{(0)}$ . Then, they move along the trajectories rapidly and reach the next temporary stationary location at  $t = 55P_{\text{out}}^{(0)}$  as the top right panel indicates. Then the orientations of the angular momenta stay in the same location until  $t \approx 105P_{\text{out}}^{(0)}$ , and reach the next location at  $t = 128P_{\text{out}}^{(0)}$ . This evolution pattern continues, while their mutual inclination  $i_{\text{mut}}$  oscillates between  $40^\circ$  and  $90^\circ$  in a regular and periodic fashion.

Independent of such complicated behavior of orbital angles, the RV variations of frequencies  $\nu_{\pm 3}$  and  $\nu_{\pm 1}$  can be used as a signature of inner binaries as indicated by the middle panels of Figure 9. This implies that we can use the same strategy to detect an inner binary as well, even for a noncoplanar system.

Just for completeness, Figures 10 and 11 show the results for noncoplanar and very unequal mass cases: I0218 and O0218. The resulting figures support that the overall behavior is very similar to equal-mass cases, except for higher-order effects, which may come from the octupole disturbing function. Since the angular momentum of the inner binary is smaller than that in equal-mass cases, the total angular momentum is dominated by that of the outer orbit. Therefore, the outer orbital inclination is more stable. The RV variations and LS periodograms confirm again that the basic strategy for detecting an inner binary is valid also for unequal-mass and noncoplanar triple systems.

Even a nondetection of such long-term RV variations induced by the precession or the KL oscillations can put constraints on the presence of the inner binary. Liu et al. (2019), for example, have

observed the LB-1 system for 7 months ( $\sim 3P_{\text{out}}^{(0)}$ ) over 1.5 years ( $\sim 7P_{\text{out}}^{(0)}$ ), and found no systematic variation in the semi-amplitude of the total RV curve more than  $\sim 1$  km/s. If a similar level of upper limits on the RV modulation is placed on a true star-BH binary, we can exclude the presence of an inner binary with moderate inclinations such as I1010 and I0218. Therefore, an inner binary, if exists, should have either near-coplanar (no appreciable precession) or very inclined (long precession timescale) orbits. For the latter case, the drastic change in semi-amplitude of the RV might be observed after a characteristic timescale of the KL oscillation  $T_{\text{KL}}$  (see Figures 9 and 11). This methodology is indeed successful at putting a constraint on the lower limit of mutual inclination for a stellar triple HD109648 from the detection of long-term RV variations:  $5.4^\circ \leq i_{\text{mut}}$  (prograde case) and  $i_{\text{mut}} \leq 174.6^\circ$  (retrograde case) (Jha et al. 2000). Although the LB-1 system is most likely a stellar binary, there may be yet undetected similar star-BH systems for which the present methodology is applicable. If an outer star of such systems has a relatively short orbital period, the longer-term monitoring of the total RV amplitude may reveal a possible noncoplanar inner binary.

Blaes et al. (2002); Liu & Lai (2017, 2018); Thompson (2011), among others, have suggested that the Kozai-Lidov oscillation acting on an inner BBH may significantly accelerate the BBH merging timescale. The detection of noncoplanar triples containing a BBH, thus, would provide very interesting opportunities to understand the formation pathway for the population of BBHs that have been continuously detected with gravitational wave signals.

#### 4. DISCUSSION

It is known that the GR precession of an inner binary suppresses the Kozai-Lidov (KL) oscillation effectively when its precession rate  $\dot{\omega}_{\text{GR}}$  exceeds the KL precession rate  $\dot{\omega}_{\text{K}}$ . Their ratio is given by

$$\frac{\dot{\omega}_{\text{GR}}}{\dot{\omega}_{\text{K}}} = \frac{3(1 - e_{\text{out}}^2)^{3/2}}{\sqrt{1 - e_{\text{in}}^2}} \left(\frac{v_{\text{in}}}{c}\right)^2 \left(\frac{P_{\text{out}}}{P_{\text{in}}}\right)^2 \frac{m_1 + m_2 + m_*}{m_*}, \quad (32)$$

where  $v_{\text{in}} \equiv \sqrt{\mathcal{G}(m_1 + m_2)/a_{\text{in}}}$  corresponds to the orbital velocity of the inner binary (e.g. Liu et al. 2015).

The left panel of Figure 12 shows the precession ratio, equation (32), against  $e_{\text{in}}$  for  $P_{\text{in}} = 1, 3, 5$  and 10 days, where we adopt the fiducial values for the other parameters. The plot indicates that the GR precession effect is safely neglected unless the inner binary is highly eccentric or has a very short orbital period. Moreover, we performed simulations for noncoplanar models in Table 1 using REBOUNDx with GR corrections, and made sure that the maximum inner eccentricity changes less than 3 % over 1000  $P_{\text{out}}^{(0)}$  for both O1010 and O0218. Thus we conclude that our results based on purely Newtonian gravity are not affected by the GR precession. The GR effect, however, might change the evolution of the triple over a much longer timescale, including the secular stability of the system. This is an interesting problem on its own, but beyond the scope of this paper. We plan to study this problem in due course using the secular perturbation theory, instead of the direct N-body approach adopted here.

The gravitational wave (GW) emission may also affect the long-term stability of the system. The GW induced merger timescale for an eccentric isolated binary is analytically given by (Peters 1964)

$$\tau_{\text{GW}} = \frac{12 c_0^4}{19 \beta} \int_0^{e_0} \frac{de e^{\frac{29}{19}} \left(1 + \frac{121}{304} e^2\right)^{\frac{1181}{2299}}}{(1 - e^2)^{3/2}}, \quad (33)$$

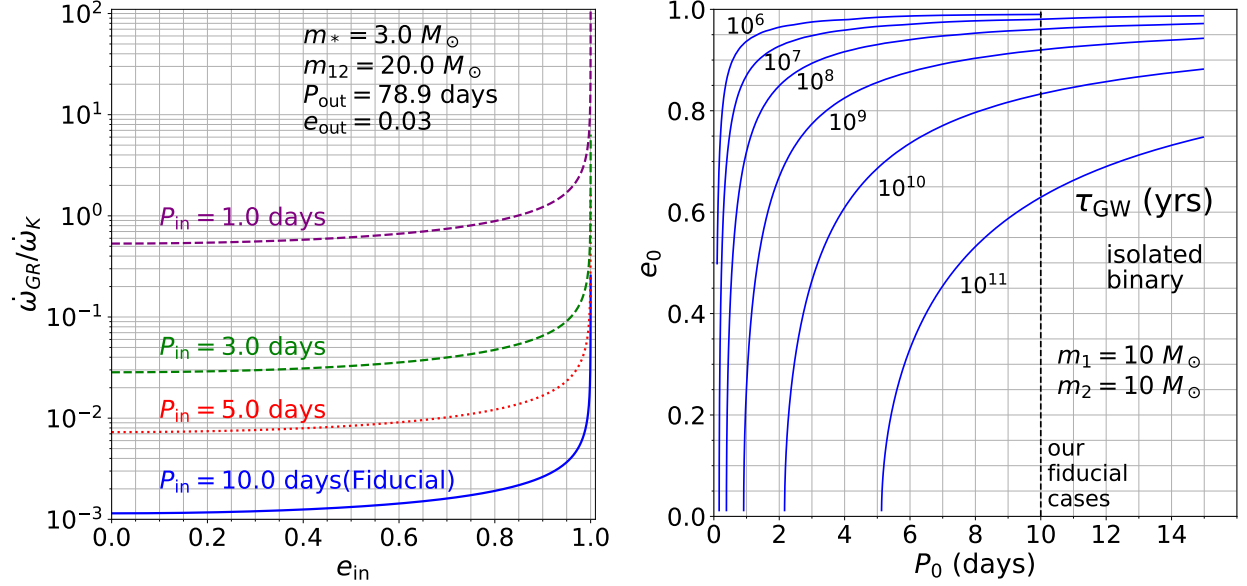


**Figure 12.** Characteristic timescales of the GR corrections. *Left:* the ratio of GR and KL precession rates  $\dot{\omega}_{\text{GR}}/\dot{\omega}_{\text{K}}$  of the inner pericenter arguments  $\omega$  against the eccentricity of the inner binary  $e_{\text{in}}$  for  $P_{\text{in}} = 1, 3, 5$  and  $10$  days. *Right:* contour plots of the merger time  $\tau_{\text{GW}}$  due to the gravitational wave emission on the  $P_0 - e_0$  plane for an isolated binary (neglecting the effect of the tertiary star).

where

$$c_0 \equiv \frac{(1 - e_0^2)}{e_0^{12/19}} \left( \frac{\mathcal{G}(m_1 + m_2)P_0^2}{4\pi^2} \right)^{1/3} \left( 1 + \frac{121}{304}e_0^2 \right)^{-\frac{870}{2299}} \quad \text{and} \quad \beta \equiv \frac{64 \text{ G}^3 m_1 m_2 (m_1 + m_2)}{5 c^5} \quad (34)$$

with  $P_0$  and  $e_0$  being the initial orbital period and eccentricity, respectively.

The right panel of Figure 12 plots the contour of  $\tau_{\text{GW}}$  as a function of the eccentricity and orbital period at the initial epoch,  $e_0$  and  $P_0$ . Again, the GW emission is largely negligible unless the binary is highly eccentric or has a very short orbital period, which is not the case for our models considered here. This estimate, however, neglects the dynamical effect by the tertiary object on the inner binary, and may vary in a case where the KL oscillation excites significantly the eccentricity of the inner binary.

It is also possible that the orbit of the outer star is affected by the inverse-KL and other eccentricity-inclination resonances (e.g. de Elía et al. 2019; Naoz et al. 2017, 2020; Vinson & Chiang 2018), which may enhance the outer eccentricity effectively, depending on the initial conditions. For example, Vinson & Chiang (2018) showed that the eccentricity of an outer test particle can be enhanced up to  $\sim 0.2$  and  $\sim 0.3$  by the inverse KL resonance and octupole resonance on  $\varpi_{\text{out}} + \varpi_{\text{in}} - 2\Omega_{\text{out}}$ , respectively. They also pointed out that the outer eccentricity enhancement becomes stronger as the inner eccentricity increases, due to the octupole apse-aligned resonance. The outer eccentricity enhancement may lead to the orbital crossing and the system may become unstable eventually.

For our fiducial cases, however, the amplitudes of the inner and outer orbital angular momenta are comparable. Thus the test particle approximation for the tertiary star is not valid. In this case, the total angular momentum conservation may prohibit the significant enhancement of the outer



eccentricity. Nevertheless, the inverse KL effect and other resonances may play an important role in the orbital evolution and secular stability of triples in certain sets of orbital parameters of the triples.

The long-term dynamical effects mentioned in the above (GW emission, normal and inverse KL oscillations, and other resonances) can also be examined by the secular perturbation analysis that we plan in future. Thus we do not discuss those further in the present paper, and we hope to report the detailed results elsewhere.

Finally, we briefly mention possible formation mechanisms of tight triples including compact binaries of our interest. In reality, however, reliable formation scenarios are very difficult to construct, while several authors proposed possible evolution channels for triple systems (e.g. [Toonen et al. 2016](#)). Since the common-envelope evolution of binary stars significantly shrinks their orbital separations, tight binaries may be produced (e.g. [Toonen et al. 2016](#); [Zorotovic et al. 2010](#)) if they survive the subsequent violent processes like supernovae. Many complex processes including, for instance, mass transfer in eccentric orbits (e.g. [Dosopoulou & Kalogera 2016](#)), mass-loss induced eccentric KL oscillation (e.g. [Shappee & Thompson 2013](#); [Michaely & Perets 2014](#)), and supernova kicks (e.g. [Pijloo et al. 2012](#); [Toonen et al. 2016](#)) have been discussed, and are recognized to play important roles in triple formation and evolution. While those formation scenarios of tight triples are still qualitative, they offer an interesting possibility that can be further examined with more quantitative long-term simulations.

In addition, the dynamical capture scenario of BBH formation (e.g. [Portegies Zwart & McMillan 2000](#); [O’Leary et al. 2009](#); [Rodriguez et al. 2016](#); [Tanikawa et al. 2020](#); [Di Carlo et al. 2020](#)) predicts the formation of temporal triples (see e.g. [Rodriguez et al. 2016](#)). Thus, the dynamical capture would also provide a possible formation channel for triple systems including BBHs although it is currently not certain if such triples could survive after escaping from the star-dense region.

## 5. CONCLUSION

It is expected that there are many star-BH binaries including unseen companions in our Galaxy (e.g. [Breivik et al. 2017](#); [Kawanaka et al. 2016](#); [Mashian & Loeb 2017](#); [Yamaguchi et al. 2018](#); [Masuda & Hotokezaka 2019](#)). A fraction of them may be a triple system comprising an inner binary black hole. Given the fact that LIGO has already detected many BBHs, it is important to search for detached BBHs hidden in such systems apart from the gravitational wave.

In the previous paper ([Hayashi et al. 2020](#)), we proposed a novel methodology for detecting an inner BBH in a triple system through the periodic RV variations of the outer star, and presented the observational feasibility using mock observations focused on coplanar triple systems. This paper has extended the study of [Hayashi et al. \(2020\)](#) and considered more generic cases of coplanar eccentric and noncoplanar inner binaries. In this paper, we adopt parameters of fiducial star-BBH triple systems largely inspired by LB-1 originally estimated by [Liu et al. \(2019\)](#); [El-Badry & Quataert \(2020\)](#); [Abdul-Masih et al. \(2020\)](#), and compute the expected RV variations using N-body simulations. Although it is now unlikely that LB-1 is a star-BH binary ([Shenar et al. 2020](#)), the results in this paper capture the basic behavior of such triples that remain to be detected in the near future.

Our main conclusions are summarized below:

(1) Coplanar inner binaries of  $P_{\text{in}} > 2$  weeks in our fiducial triples with a few month outer orbital period are ruled out by the dynamical stability condition. Conversely, an inner BBH of  $P_{\text{in}} \approx 1$  week should add an RV variation on the order of 100 m/s at roughly twice the orbital frequency of the inner binary.



(2) If a quasi-Kepler RV component on the order of 100 km/s at the outer orbital frequency is properly removed from the entire RV curve, the residual RV variation can provide direct signatures of, or useful constraints on, the presence of the inner binary.

(3) For coplanar triple systems, the shift of the outer pericenter argument  $\omega_{\text{out}}$  can be used to detect the inner binary. This is basically the same idea as a hypothetical planet Vulcan inside Mercury's orbit (Le Verrier 1859).

(4) For noncoplanar triple systems, the total RV semi-amplitude is modulated periodically by the precession of the inner and outer orbits over roughly the Kozai-Lidov oscillation timescale. The amplitude of the secular modulation depends on the observer's line of sight, but can be on the order of 100 km/s in principle. The modulation timescale is usually long, but if the outer orbital period is relatively short, to the order of months, it is quite feasible to detect over 10 years for instance. In addition, the RV variation at roughly twice the orbital frequency of the inner binary may be searched via short-cadence monitoring of the system, although the behavior of the short-term RV variation becomes complicated for noncoplanar triples. Incidentally, we note here that Jha et al. (2000) detected the RV semi-amplitude variation for a tight stellar triple HD109648, due to its nodal precession over their 8 yr RV observation. Thus the similar detection for star-BBH triples should be quite feasible.

As we have stressed before, our proposed strategy to search for an inner binary in a triple system is quite generic. Even though we adopt fiducial parameters of triple systems in this paper according to the previous interpretation for the LB-1 system by Liu et al. (2019), our methodology can be readily applied to numerous star-black hole systems that are expected to be discovered in the near future. Currently, there are many proposals to search for star-black hole binaries with Gaia (e.g. Breivik et al. 2017; Kawanaka et al. 2016; Mashian & Loeb 2017; Yamaguchi et al. 2018; Shikauchi et al. 2020) and TESS (Masuda & Hotokezaka 2019). For instance, Yamaguchi et al. (2018) predict that hundreds of such binaries will be discovered with Gaia in its 5 year observation. Masuda & Hotokezaka (2019) point out that dozens of star-black hole systems would be detected through the detailed analyses of TESS light curves. Therefore, the detected number of star-black hole systems could increase significantly in the near future. Any other future observational missions should also contribute much to such discoveries.

The dynamics of triple systems that we described here can be applied to various other methods for detecting interesting astronomical systems. For instance, probing the dynamics of binary pulsars in triple systems using the pericenter shift (e.g. Suzuki et al. 2019), the RV variation of a star passing close to unseen companions, and the search for binary planets (e.g. Lewis et al. 2015; Ochiai et al. 2014) in known exoplanetary systems.

Finally, we would like to emphasize that the strategy proposed here is no longer just a theoretical idea, but becomes an observationally feasible methodology for searching for otherwise unseen astrophysical objects. In the near future, this methodology is expected to help in detecting not-yet-known populations of astronomical objects.

## ACKNOWLEDGMENTS

We thank an anonymous referee for several useful comments. Simulations and analyses in this paper made use of `REBOUND`, `RadVel`, and `Astropy`. We gratefully acknowledge the support from Grants-in-Aid for Scientific Research by the Japan Society for Promotion of Science (JSPS) No.18H01247 and No.19H01947, and from JSPS Core-to-core Program “International Network of Planetary Sciences”.

*Software:* `Astropy` (Astropy Collaboration et al. 2013, 2018), `RadVel` (Fulton et al. 2018), `REBOUND` (Rein & Liu 2012)

## APPENDIX

## A. THE SECULAR LAGRANGE PLANETARY EQUATIONS FOR A TRIPLE SYSTEM CONSISTING OF AN INNER BINARY AND A TERTIARY STAR

The noncoplanar results shown in subsection 3.4 exhibit a precession-like behavior. We discuss the secular evolution of orbital angles in noncoplanar triples from the Lagrange planetary equations.

The orbit-averaged quadrupole Hamiltonian  $\bar{F}$  is given by (e.g., Morais & Correia 2012):

$$\bar{F} = C_{\text{quad}} [2 - 12e_{\text{in}}^2 - 6(1 - e_{\text{in}}^2)(\sin I_{\text{in}} \sin I_{\text{out}} \cos(\Delta\Omega) + \cos I_{\text{in}} \cos I_{\text{out}})^2 + 30e_{\text{in}}^2 \times (-\sin I_{\text{out}} \cos I_{\text{in}} \sin \omega_{\text{in}} \cos(\Delta\Omega) - \sin I_{\text{out}} \cos \omega_{\text{in}} \sin(\Delta\Omega) + \sin I_{\text{in}} \sin \omega_{\text{in}} \cos I_{\text{out}})^2], \quad (\text{A1})$$

where

$$C_{\text{quad}} \equiv \frac{\mathcal{G}}{16} \frac{m_1 m_2}{m_1 + m_2} \frac{m_*}{(1 - e_{\text{out}}^2)^{3/2}} \left( \frac{a_{\text{in}}^2}{a_{\text{out}}^3} \right), \quad (\text{A2})$$

$$\Delta\Omega \equiv \Omega_{\text{in}} - \Omega_{\text{out}}. \quad (\text{A3})$$

In equation (A2) and throughout this appendix, we denote Newton’s gravitational constant by  $\mathcal{G}$ , since  $G$  indicates a canonical variable corresponding to an orbital angular momentum.

With the orbit-averaged Hamiltonian  $\bar{F}$ , the secular evolution of orbital angles is explicitly written as (e.g. Danby 1988; Murray & Dermott 2000; Valtonen & Karttunen 2006)

$$\dot{\omega}_j = -\frac{\sqrt{1 - e_j^2}}{\mu_j \nu_j a_j^2 e_j} \frac{\partial \bar{F}}{\partial e_j} + \frac{\cos I_j}{\mu_j \nu_j a_j^2 \sqrt{1 - e_j^2} \sin I_j} \frac{\partial \bar{F}}{\partial I_j}, \quad (\text{A4})$$

$$\dot{\Omega}_j = -\frac{1}{\mu_j \nu_j a_j^2 \sqrt{1 - e_j^2} \sin I_j} \frac{\partial \bar{F}}{\partial I_j}, \quad (\text{A5})$$

$$\dot{I}_j = \frac{1}{\mu_j \nu_j a_j^2 \sqrt{1 - e_j^2} \sin I_j} \frac{\partial \bar{F}}{\partial \Omega_j} - \frac{\cos I_j}{\mu_j \nu_j a_j^2 \sqrt{1 - e_j^2} \sin I_j} \frac{\partial \bar{F}}{\partial \omega_j}, \quad (\text{A6})$$

where  $j$ (= in and out). We define the corresponding reduced mass as

$$\mu_{\text{in}} \equiv \frac{m_1 m_2}{m_1 + m_2}, \quad (\text{A7})$$

$$\mu_{\text{out}} \equiv \frac{m_*(m_1 + m_2)}{m_1 + m_2 + m_*}. \quad (\text{A8})$$

We note that the Lagrange planetary equations are often written in terms of the disturbing function  $R \equiv -\bar{F}$  (e.g. Murray & Dermott 2000).

Neglecting the  $\mathcal{O}(e_{\text{in}}^2)$  terms in equation (A1), equations (A4), (A5), and (A6) for  $j = \text{in, out}$  are explicitly written as follows:

$$\dot{\omega}_{\text{in}} = \frac{12C_{\text{quad}}(1 - e_{\text{in}}^2)}{G_{\text{in}}} \left[ 2 - \cos^2 i_{\text{mut}} - \frac{\cos I_{\text{in}}}{\sin I_{\text{in}}} \cos i_{\text{mut}} (\cos I_{\text{in}} \sin I_{\text{out}} \cos \Delta\Omega - \sin I_{\text{in}} \cos I_{\text{out}}) - 5(-\sin I_{\text{out}} \cos I_{\text{in}} \sin \omega_{\text{in}} \cos(\Delta\Omega) - \sin I_{\text{out}} \cos \omega_{\text{in}} \sin(\Delta\Omega) + \sin I_{\text{in}} \sin \omega_{\text{in}} \cos I_{\text{out}})^2 \right] \quad (\text{A9})$$

$$\dot{\omega}_{\text{out}} = \frac{6C_{\text{quad}}}{G_{\text{out}}} \left[ (3 \cos^2 i_{\text{mut}} - 1) - 2 \frac{\cos I_{\text{out}}}{\sin I_{\text{out}}} \cos i_{\text{mut}} (\sin I_{\text{in}} \cos I_{\text{out}} \cos \Delta\Omega - \cos I_{\text{in}} \sin I_{\text{out}}) \right], \quad (\text{A10})$$

$$\dot{\Omega}_{\text{in}} = \frac{12C_{\text{quad}}}{G_{\text{in}} \sin I_{\text{in}}} \cos i_{\text{mut}} (\cos I_{\text{in}} \sin I_{\text{out}} \cos \Delta\Omega - \sin I_{\text{in}} \cos I_{\text{out}}), \quad (\text{A11})$$

$$\dot{\Omega}_{\text{out}} = \frac{12C_{\text{quad}}}{G_{\text{out}} \sin I_{\text{out}}} \cos i_{\text{mut}} (\sin I_{\text{in}} \cos I_{\text{out}} \cos \Delta\Omega - \cos I_{\text{in}} \sin I_{\text{out}}), \quad (\text{A12})$$

$$\dot{I}_{\text{in}} = \frac{12C_{\text{quad}}}{G_{\text{in}}} \cos i_{\text{mut}} \sin I_{\text{out}} \sin \Delta\Omega, \quad (\text{A13})$$

$$\dot{I}_{\text{out}} = -\frac{12C_{\text{quad}}}{G_{\text{out}}} \cos i_{\text{mut}} \sin I_{\text{in}} \sin \Delta\Omega, \quad (\text{A14})$$

where  $G_{\text{in}}$  and  $G_{\text{out}}$  are the angular momenta of the inner and outer orbits defined as

$$G_{\text{in}} \equiv \mu_{\text{in}} \nu_{\text{in}} a_{\text{in}}^2 \sqrt{1 - e_{\text{in}}^2}, \quad (\text{A15})$$

$$G_{\text{out}} \equiv \mu_{\text{out}} \nu_{\text{out}} a_{\text{out}}^2 \sqrt{1 - e_{\text{out}}^2}. \quad (\text{A16})$$

Note that we use an arbitrary inertial frame to write down the equations, rather than the invariant plane. Equation (A10) reduces to equation (18) for coplanar prograde ( $\Delta\Omega = 0$  and  $I_{\text{in}} = I_{\text{out}}$ ) and retrograde ( $\Delta\Omega = \pi$  and  $I_{\text{in}} = \pi + I_{\text{out}}$ ) systems.

Consider first the case of moderate mutual inclination  $i_{\text{mut}}$  and small inner eccentricity  $e_{\text{in}}$ , in which the Kozai-Lidov (KL) oscillation is not so effective and  $e_{\text{in}}$  remains negligibly small. In this case, the secular evolution is basically described by the precession of the inner and outer angular momenta around the total angular momentum axis with  $G_{\text{in}}$ ,  $G_{\text{out}}$ , and  $G_{\text{tot}}$  being constant, where

$$G_{\text{tot}} = \sqrt{G_{\text{in}}^2 + G_{\text{out}}^2 + 2G_{\text{in}}G_{\text{out}} \cos i_{\text{mut}}}. \quad (\text{A17})$$

Indeed such motion well explains those of I1010 and I0218, where the normal directions of orbits move on the circles centered at the total angular momentum direction.

Thus, its precession timescale can be computed by considering the motion with respect to the invariant reference frame ( $\Delta\Omega = \pi$ ,  $i_{\text{mut}} = I_{\text{in}} + I_{\text{out}}$ ). Since  $G_{\text{in}}/\sin I_{\text{out}} = G_{\text{out}}/\sin I_{\text{in}} = G_{\text{tot}}/\sin I_{\text{mut}}$  holds in this case, equations (A11) and (A12) reduce to

$$\dot{\Omega}_j = -\frac{12C_{\text{quad}}G_{\text{tot}}}{G_{\text{in}}G_{\text{out}}} \cos i_{\text{mut}}. \quad (\text{A18})$$

The precession rate above is constant if we neglect the higher-order variation of mutual inclination, and it is expressed analytically as

$$P_{\Omega} = \frac{2\pi}{\dot{\Omega}} = \frac{\pi G_{\text{in}}G_{\text{out}}}{6C_{\text{quad}}G_{\text{tot}} \cos i_{\text{mut}}}. \quad (\text{A19})$$

**Table 3.** Parameters relevant to precession timescales for fiducial noncoplanar models

case	$i_{\text{mut}}$ (deg)	$G_{\text{in}}/C_{\text{quad}}P_{\text{out}}^{(0)}$	$G_{\text{out}}/C_{\text{quad}}P_{\text{out}}^{(0)}$	$G_{\text{tot}}/C_{\text{quad}}P_{\text{out}}^{(0)}$	$P_{\Omega}/P_{\text{out}}^{(0)}$
I1010	45	153.8	175.3	304.2	65.6
O1010	90	153.8	175.3	233.2	$+\infty$
I0218	45	153.8	486.9	605.6	91.6
O0218	90	153.8	486.9	510.7	$+\infty$

If we neglect the  $\mathcal{O}(e_{\text{in}}^2)$  and  $\mathcal{O}(e_{\text{out}}^2)$  terms, equation (A19) is further approximated as

$$\frac{P_{\Omega}}{P_{\text{out}}} \approx \frac{80.7}{\cos i_{\text{mut}}} \left( \frac{m_1 + m_2 + m_*}{23 M_{\odot}} \right) \left( \frac{m_*}{3 M_{\odot}} \right)^{-1} \left( \frac{P_{\text{out}}}{78.9 \text{ days}} \right) \left( \frac{P_{\text{in}}}{10.0 \text{ days}} \right)^{-1} \quad (\text{A20})$$

for  $G_{\text{out}} \gg G_{\text{in}}$ , and

$$\frac{P_{\Omega}}{P_{\text{out}}} \approx \frac{92.0}{\cos i_{\text{mut}}} \frac{(m_1 + m_2)^2}{4m_1m_2} \left( \frac{m_1 + m_2 + m_*}{23 M_{\odot}} \right)^{\frac{2}{3}} \left( \frac{m_1 + m_2}{20 M_{\odot}} \right)^{-\frac{2}{3}} \left( \frac{P_{\text{out}}}{78.9 \text{ days}} \right)^{\frac{4}{3}} \left( \frac{P_{\text{in}}}{10.0 \text{ days}} \right)^{-\frac{4}{3}} \quad (\text{A21})$$

for  $G_{\text{out}} \ll G_{\text{in}}$ . We compute the periods for our four noncoplanar models (in which  $G_{\text{out}} \sim G_{\text{in}}$ ) from equation (A19). The values summarized in Table 3 are in reasonable agreement with the results shown in Figures 8 and 10. For comparison, we write down the conventional KL timescale for an inner test particle (e.g. Merritt 2013):

$$\begin{aligned} \frac{T_{\text{KL}}}{P_{\text{out}}} &= \frac{m_1}{m_*} \left( \frac{P_{\text{out}}}{P_{\text{in}}} \right) (1 - e_{\text{out}}^2)^{3/2} \\ &\approx 26 \left( \frac{m_1}{10 M_{\odot}} \right) \left( \frac{m_*}{3 M_{\odot}} \right)^{-1} \left( \frac{P_{\text{out}}}{78.9 \text{ days}} \right) \left( \frac{P_{\text{in}}}{10 \text{ days}} \right)^{-1} (e_{\text{out}}^2 \ll 1). \end{aligned} \quad (\text{A22})$$

The timescale roughly agrees with equation (A20) within order estimation.

While the orbital inclinations  $I_{\text{in}}$  and  $I_{\text{out}}$  are constant in the invariant reference frame, i.e., defined with respect to the total angular momentum axis, they also exhibit periodic variations due to the  $\Omega$  precessions for an arbitrary line of sight. Thus the period of inclination variations is also given by equation (A19), which basically explains the behavior of I1010 and I0218 shown in Figures 8 and 10.

Consider next a larger mutual inclination like O1010 and O0218. In this case, the KL oscillation is efficient and increases the inner eccentricity significantly and periodically. Since the precession period, equation (A19), is inversely proportional to  $\cos i_{\text{mut}}$ , the timescale of the inclination change is very sensitive to the value of  $i_{\text{mut}}$ . As shown in Figures 9 and 11, O1010 and O0218 spend most of their time around  $i_{\text{mut}} \approx \pi/2$ . Then the KL oscillation gradually enhances the inner eccentricity, and drastically changes the inclinations. During such transient time,  $i_{\text{mut}}$  becomes very small, but rapidly goes back to  $\approx \pi/2$  again.

A more quantitative estimate of the corresponding period is difficult and generally requires numerical integration of a set of the Lagrange planetary equations including the eccentricity terms, although several analytical and numerical results have been presented in previous literature (e.g. Kinoshita & Nakai 1999; Merritt 2013; Naoz et al. 2013; Antognini 2015; Will 2017; Vinson & Chiang 2018).

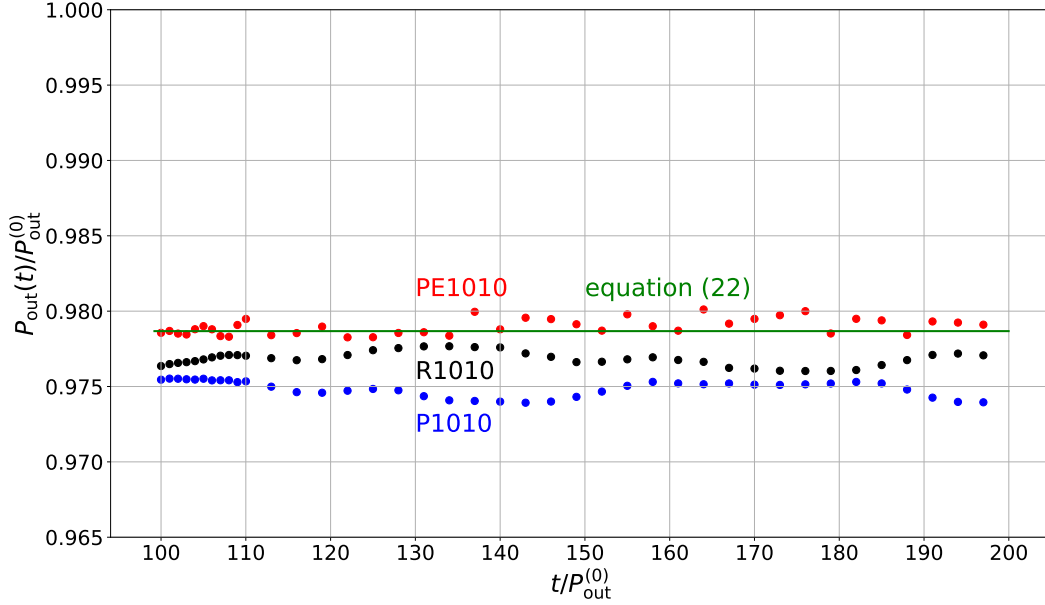


**Figure B1.** Best-fit values of  $P_{\text{out}}(t_n \equiv nP_{\text{out}}^{(0)})$  for coplanar systems. They are estimated with RadVel using the 0.1 day cadence simulated RV data over  $nP_{\text{out}}^{(0)} < t < (n+1)P_{\text{out}}^{(0)}$  for  $100 \leq n < 200$ ; P1010 (blue), R1010 (black), and PE1010 (red). The solid green line indicates the analytic prediction (see equation (22) in Appendix B).

## B. ORBITAL PERIOD OF A MODULATED KEPLERIAN MOTION

Equation (22) in the main text incorrectly ignored the time dependence of the initial true anomaly  $f_{\text{out}}^{(0)}(t)$  in the approximation. The correct version of the equation should read

$$\frac{P_{\text{out}}(t)}{P_{\text{out}}^{(0)}} \approx \frac{2\pi}{\nu_{\text{out}} + \dot{\omega}_{\text{out}} + f_{\text{out}}^{(0)}} \approx 1 - \frac{2\dot{\omega}_{\text{out}}P_{\text{out}}}{2\pi} \approx 0.978, \quad (22)$$

where  $\dot{\omega}_{\text{out}}$  is the precession rate of the outer pericenter argument  $\omega_{\text{out}}$ . The detailed discussion of the approximation is described in appendix of Hayashi & Suto (2021). As a result,  $1 - P_{\text{out}}(t)/P_{\text{out}}^{(0)}$  becomes twice larger than that predicted in Figure 4 in the main text. Figure 4 should be replaced by Figure B1 after this correction.

## C. THE DETAILED EVOLUTION OF MUTUAL INCLINATION IN FIGURE 8

In order to clarify the detailed evolution of mutual inclination in Figure 8, we here show the enlarged version of the top right panel of Figure 8. Figure C1 shows enlarged panels of the evolution of mutual inclination for I1010. The first, second, third, and fourth panels show the evolution over  $0 - 1000P_{\text{out}}$ ,  $0 - 50P_{\text{out}}$ ,  $0 - 10P_{\text{out}}$ , and  $0 - 1.0P_{\text{out}}$ , respectively.

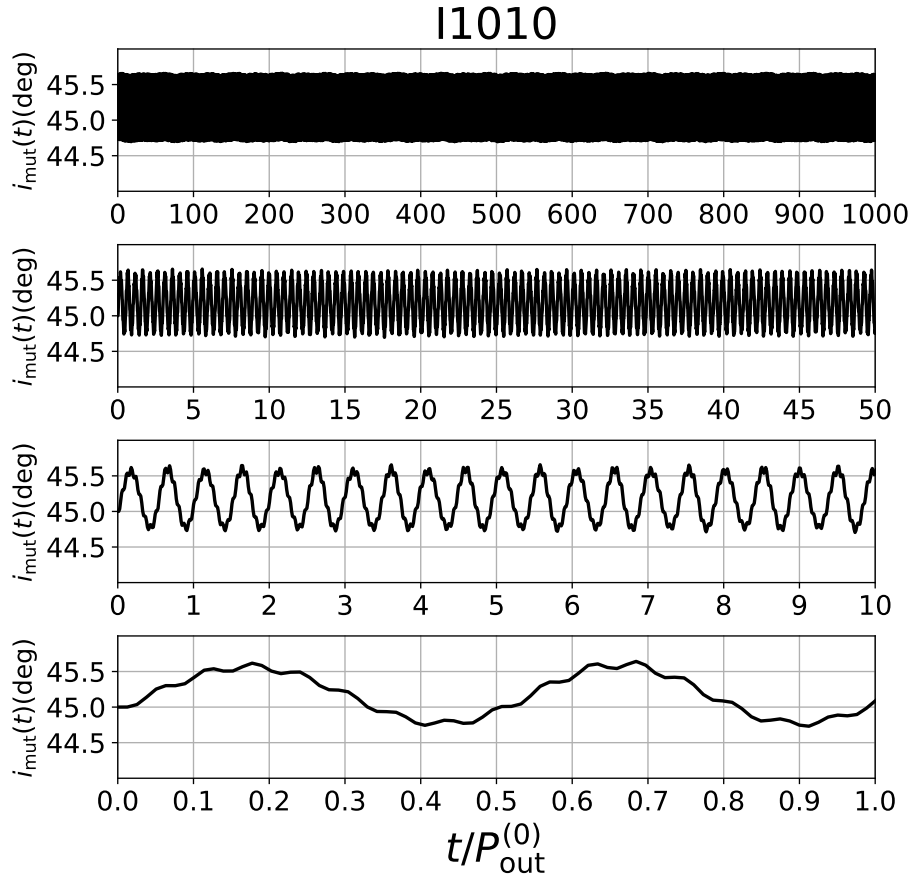


**Figure C1.** The enlarged plot of the top right panel of Figure 8 for I1010 in order to clarify the detailed evolution of mutual inclination. The first, second, third, and fourth panels from top show the evolution over  $0 - 1000P_{\text{out}}$ ,  $0 - 50P_{\text{out}}$ ,  $0 - 10P_{\text{out}}$ , and  $0 - 1.0P_{\text{out}}$ , respectively.

## REFERENCES

- Aarseth, S. J., & Mardling, R. A. 2001, *Astronomical Society of the Pacific Conference Series*, Vol. 229, *The Formation and Evolution of Multiple Star Systems*, ed. P. Podsiadlowski, S. Rappaport, A. R. King, F. D’Antona, & L. Burderi, 77
- Abbott, B. P., Abbott, R., Abbott, T. D., et al. 2016, *Physical Review Letters*, 116, 061102
- Abdul-Masih, M., Banyard, G., Bodensteiner, J., et al. 2020, *Nature*, 580, E11
- Antognini, J. M. O. 2015, *MNRAS*, 452, 3610
- Astropy Collaboration, Robitaille, T. P., Tollerud, E. J., et al. 2013, *A&A*, 558, A33
- Astropy Collaboration, Price-Whelan, A. M., Sipócz, B. M., et al. 2018, *AJ*, 156, 123
- Blaes, O., Lee, M. H., & Socrates, A. 2002, *ApJ*, 578, 775
- Breivik, K., Chatterjee, S., & Larson, S. L. 2017, *ApJL*, 850, L13
- Danby, J. M. A. 1988, *Fundamentals of celestial mechanics* (Willmann-Bell, Inc.)
- de Elía, G. C., Zanardi, M., Dugaro, A., & Naoz, S. 2019, *A&A*, 627, A17
- Di Carlo, U. N., Mapelli, M., Giacobbo, N., et al. 2020, arXiv e-prints, arXiv:2004.09525. <https://arxiv.org/abs/2004.09525>
- Dosopoulou, F., & Kalogera, V. 2016, *ApJ*, 825, 71
- Einstein, A. 1915, *Sitzungsber. preuss. Akad. Wiss.*, 47, 831
- El-Badry, K., & Quataert, E. 2020, *MNRAS*, 493, L22
- Fulton, B. J., Petigura, E. A., Blunt, S., & Sinukoff, E. 2018, *PASP*, 130, 044504
- Harrington, R. S. 1972, *Celestial Mechanics*, 6, 322

- Hayashi, T., Wang, S., & Suto, Y. 2019, A strategy to search for an inner binary black hole from the motion of the tertiary star I: a perturbative analytic approach to a coplanar and near-circular three-body system and its application to 2M05215658+4359220.  
<https://arxiv.org/abs/1905.07100v1>
- . 2020, *The Astrophysical Journal*, 890, 112
- . 2021, *The Astrophysical Journal*, 907, 48
- Jha, S., Torres, G., Stefanik, R. P., Latham, D. W., & Mazeh, T. 2000, *MNRAS*, 317, 375
- Kawanaka, N., Yamaguchi, M., Piran, T., & Bulik, T. 2016, *Proceedings of the International Astronomical Union*, 12, 41
- Kinoshita, H., & Nakai, H. 1999, *Celestial Mechanics and Dynamical Astronomy*, 75, 125
- Kobulnicky, H. A., Kiminki, D. C., Lundquist, M. J., et al. 2014, *ApJS*, 213, 34
- Kozai, Y. 1962, *AJ*, 67, 591
- Le Verrier, U.-J. 1859, *Comptes rendus hebdomadaires des séances de l'Académie des sciences*, 49, 379
- Leung, S.-C., Nomoto, K., & Blinnikov, S. 2019, *ApJ*, 887, 72
- Lewis, K. M., Ochiai, H., Nagasawa, M., & Ida, S. 2015, *ApJ*, 805, 27
- Lidov, M. L. 1962, *Planet. Space Sci.*, 9, 719
- Liu, B., & Lai, D. 2017, *ApJL*, 846, L11
- . 2018, *ApJ*, 863, 68
- Liu, B., Muñoz, D. J., & Lai, D. 2015, *MNRAS*, 447, 747
- Liu, J., Zhang, H., Howard, A. W., et al. 2019, *Nature*, 575, 618
- Mardling, R., & Aarseth, S. 1999, in *NATO Advanced Science Institutes (ASI) Series C*, Vol. 522, *NATO Advanced Science Institutes (ASI) Series C*, ed. B. A. Steves & A. E. Roy (Springer), 385
- Mardling, R. A. 2013, *MNRAS*, 435, 2187
- Mardling, R. A., & Aarseth, S. J. 2001, *MNRAS*, 321, 398
- Mashian, N., & Loeb, A. 2017, *MNRAS*, 470, 2611
- Masuda, K., & Hotokezaka, K. 2019, *ApJ*, 883, 169
- Mayor, M., & Queloz, D. 1995, *Nature*, 378, 355
- Merritt, D. 2013, *Dynamics and Evolution of Galactic Nuclei* (Princeton University Press)
- Michaely, E., & Perets, H. B. 2014, *ApJ*, 794, 122
- Morais, M. H. M., & Correia, A. C. M. 2008, *A&A*, 491, 899
- . 2011, *A&A*, 525, A152
- . 2012, *MNRAS*, 419, 3447
- Murray, C. D., & Dermott, S. F. 2000, *Solar System Dynamics* (Cambridge University Press)
- Naoz, S., Farr, W. M., Lithwick, Y., Rasio, F. A., & Teyssandier, J. 2013, *MNRAS*, 431, 2155
- Naoz, S., Li, G., Zanardi, M., de Elía, G. C., & Di Sisto, R. P. 2017, *AJ*, 154, 18
- Naoz, S., Will, C. M., Ramirez-Ruiz, E., et al. 2020, *ApJL*, 888, L8
- Newhall, X. X., Standish, E. M., & Williams, J. G. 1983, *A&A*, 125, 150
- Ochiai, H., Nagasawa, M., & Ida, S. 2014, *ApJ*, 790, 92
- O'Leary, R. M., Kocsis, B., & Loeb, A. 2009, *MNRAS*, 395, 2127
- Peters, P. C. 1964, *Physical Review*, 136, 1224
- Pijloo, J. T., Caputo, D. P., & Portegies Zwart, S. F. 2012, *MNRAS*, 424, 2914
- Portegies Zwart, S. F., & McMillan, S. L. W. 2000, *ApJL*, 528, L17
- Raghavan, D., McAlister, H. A., Henry, T. J., et al. 2010, *ApJS*, 190, 1
- Rein, H., & Liu, S. F. 2012, *A&A*, 537, A128
- Rein, H., & Tamayo, D. 2015, *MNRAS*, 452, 376
- Rodriguez, C. L., Haster, C.-J., Chatterjee, S., Kalogera, V., & Rasio, F. A. 2016, *ApJL*, 824, L8
- Rose, S. C., Naoz, S., & Geller, A. M. 2019, *MNRAS*, 488, 2480
- Sana, H., de Mink, S. E., de Koter, A., et al. 2012, *Science*, 337, 444
- Shappee, B. J., & Thompson, T. A. 2013, *ApJ*, 766, 64
- Shen, R. F., Matzner, C. D., Howard, A. W., & Zhang, W. 2019, *arXiv e-prints*, arXiv:1911.12581.  
<https://arxiv.org/abs/1911.12581>
- Shenar, T., Bodensteiner, J., Abdul-Masih, M., et al. 2020, *arXiv e-prints*, arXiv:2004.12882.  
<https://arxiv.org/abs/2004.12882>
- Shikauchi, M., Kumamoto, J., Tanikawa, A., & Fujii, M. S. 2020, *PASJ*
- Suzuki, H., Gupta, P., Okawa, H., & Maeda, K.-i. 2019, *MNRAS*, 486, L52
- Tamayo, D., Rein, H., Shi, P., & Hernandez, D. M. 2020, *MNRAS*, 491, 2885
- Tanikawa, A., Kinugawa, T., Kumamoto, J., & Fujii, M. S. 2020, *PASJ*
- Thompson, T. A. 2011, *ApJ*, 741, 82



- Tokovinin, A. 2008, MNRAS, 389, 925
- Toonen, S., Hamers, A., & Portegies Zwart, S. 2016, Computational Astrophysics and Cosmology, 3, 6
- Valtonen, M., & Karttunen, H. 2006, The Three-Body Problem (Cambridge University Press)
- Vinson, B. R., & Chiang, E. 2018, MNRAS, 474, 4855
- Will, C. M. 2017, PhRvD, 96, 023017
- Yamaguchi, M. S., Kawanaka, N., Bulik, T., & Piran, T. 2018, ApJ, 861, 21
- Zorotovic, M., Schreiber, M. R., Gänsicke, B. T., & Nebot Gómez-Morán, A. 2010, A&A, 520, A86